energies

MDPI

Article

A Coordinated Active–Reactive Power Optimization Method for Renewable Energy Bases Considering Terminal Voltage Security and Network Loss

Yeping Yin [1,2], Ping Zhang [2], Gengning Ying [2], Bin Niu [2], Dongxu Yao [1], Boyuan Yu [1] and Zhen He [1,*]

[1] College of Electrical Engineering, Zhejiang University, Hangzhou 310027, China; yibbin@139.com (Y.Y.); 22560174@zju.edu.cn (D.Y.); yby0293@zju.edu.cn (B.Y.)
[2] Huadian Electric Power Research Institute Co., Ltd., Hangzhou 310030, China; ping-zhang@chder.com (P.Z.); gengning-yin@chder.com (G.Y.); bin-niu@chder.com (B.N.)
* Correspondence: hezhen_hz@zju.edu.cn; Tel.: +86-15623052714

Abstract

In integrated wind–PV–storage renewable energy bases, the constituent stations are electrically coupled to a significant degree. At the same time, the temporal mismatch between the active-power delivery schedule issued by the dispatch center and the available wind and PV generation, compounded by the uneven voltage profile produced by collector-line impedance, readily drives the terminal voltage of end-of-feeder turbines beyond its limit. This paper proposes a coordinated active–reactive power optimization method that jointly addresses turbine terminal voltage security and network loss. The method treats battery charging and discharging, wind and PV output, and the reactive power of every source as the decision variables of a single global optimization, convexifies the problem through a second-order cone relaxation, and thereby balances the allocation of active and reactive power. A model predictive control framework then coordinates the cross-period scheduling of storage together with the reactive power of all sources. Case studies show that, compared with conventional unified power factor control, the proposed method raises the level of terminal voltage security and lowers system network loss while still satisfying the dispatch command tracking requirement.

Keywords: renewable energy base; multi-station coordination; active–reactive power coordinated optimization; second-order cone programming; model predictive control

Check for updates

Academic Editor: David Schoenwald

Received: 20 June 2026
Revised: 24 July 2026
Accepted: 27 July 2026
Published: 29 July 2026

Copyright: © 2026 by the authors. Licensee MDPI, Basel, Switzerland. This article is an open access article distributed under the terms and conditions of the Creative Commons Attribution (CC BY) license.

1. Introduction

Driven by the "dual-carbon" goals, the desert and Gobi regions of northwestern China have become the core areas for the large-scale, concentrated development of wind and photovoltaic (PV) power, and several ten-gigawatt-scale renewable energy bases have already been commissioned [1,2]. To smooth the strong randomness of wind and PV output and to improve the controllability of large-scale grid integration and delivery [3,4], such bases are generally configured as integrated wind–PV–storage plants equipped with large-scale electrochemical storage [5,6] and connected to the grid through a long-distance corridor [7]. When this export corridor is realized by a modular multilevel converter-based high-voltage direct current system, its secure operation under DC-side faults is a further prerequisite for the reliable delivery of the base [8–10]. Unlike a single plant, a large base is typically formed by several step-up stations coupled in series or aggregated through 220 kV lines. Each station not only receives its own upper-level dispatch commands; its

reactive output and power flow also interact through the tie line, so the base behaves as one electrically coupled system [11]. Under the combined influence of collector-line impedance and the electrical distance between turbines, the terminal voltage of end-of-feeder turbines may rise markedly even when the point of common coupling (PCC) voltage is held within its commanded range. Under meteorological disturbances, the resulting terminal overvoltage can trip turbines and threaten the security and economy of system operation [12,13]. Tracking the automatic voltage control (AVC) reactive-power command and the active-power delivery schedule must therefore be accompanied by an explicit terminal voltage security constraint and by a full account of the electrical coupling between stations.

A renewable energy base usually has to respond to two kinds of upper-level dispatch at once: the reactive-power command issued by the AVC master station, and the active-power delivery schedule sent by the dispatch center [14]. References [15–17] established regulation models for several reactive sources, including PV inverters, static var generators (SVGs), and electrochemical storage, but they mostly treat storage as an instantaneous reactive source and do not capture the temporal coupling of its state of charge or the mutual exclusivity of active and reactive power within the capability circle. Reference [18] explained the reactive-regulation mechanism of doubly fed induction generators and a station-level voltage control strategy, but it relies on a station equivalent and can hardly reflect how the distribution of intra-station line parameters affects terminal voltage. References [19,20] provided reactive-allocation methods that account for the reactive margin of the turbines, yet they do not jointly coordinate active-power curtailment with reactive regulation. References [21,22] proposed turbine-level reactive-allocation methods for wind farms, but they neither consider the coupling with the active-power delivery schedule nor address coordination among multiple stations.

Wind turbines are connected to one another through collector feeders whose impedance cannot be neglected, so the reactive output of a turbine has a marked effect on both the feeder voltage profile and the operating network loss. Unified power factor control, which aims at PCC voltage tracking, has become the engineering baseline for wind farms, but it is restricted to a single type of plant and regulates reactive power only, covering neither the wind–PV–storage hybrid nor the multi-station coupling scenario. References [23,24] further incorporate terminal voltage and network loss into a multi-objective optimization, yet they mostly evaluate terminal safety through binary indices such as the number of nodes that exceed the limit, and they fail to quantify the margin of the terminal voltage relative to the trip threshold. When the terminal voltage operates close to the trip threshold for a long time, its safety margin against disturbances is clearly insufficient. In summary, the intra-station feeder voltage profile, the operating network loss, and the terminal voltage safety margin should all be treated as primary considerations of the optimal control.

Because wind and PV turbines usually operate under maximum power point tracking (MPPT), the economic operation of the base is no longer a conventional dispatch problem but a class of optimal power flow (OPF) problem; the AC OPF is intrinsically a nonlinear and nonconvex problem that is hard to solve in polynomial time. For the output optimization of renewable plants, heuristic algorithms [25,26] are widely applied, but they tend to fall into local optima and to be time-consuming. Benefiting from advances in convex optimization, the convex relaxation that recasts the original OPF as a second-order cone program (SOCP) [27–29] can obtain the global optimum in polynomial time, and both its speed and its accuracy meet the needs of station-level online control. SOCP and MPC are established techniques in renewable-plant control. DistFlow/SOCP has previously been applied to collector-side optimal power flow and loss-minimizing reactive-power dispatch in individual wind farms [30,31]. MPC has also been used for coordinated active

and reactive control of a DFIG wind farm equipped with distributed energy storage systems [32], for two-tier active–reactive coordination of a VSC–HVDC-connected wind-farm cluster [33], and for terminal-voltage control using wind turbines, energy storage, and SVG support [34]. Moreover, a closely related earlier study from our group developed a two-layer SOCP scheme for coordinating PCC voltage tracking and generator-terminal voltage security within a single wind farm [35]. Therefore, neither SOCP nor MPC, nor their simple combination, is claimed as the novelty of this study. The representative studies reviewed above focus on either an individual wind farm or a hierarchically coordinated wind-farm cluster. In contrast, the present work formulates the operation of two wind–PV–storage stations connected in series at the 220 kV level as one base-wide optimization problem. Both collector networks, the inter-station tie line, and the shared export corridor are retained in a single DistFlow tree, while each station has its own active- and reactive-power tracking terms and the storage units are coupled across time through their SOC dynamics. The methodological advance therefore lies in this unified formulation and coordination of the electrically coupled multi-station system, with SOCP and MPC serving as the tractable solution and receding-horizon implementation tools, respectively. Recent uncertainty-aware power-system research includes probabilistic voltage-security assessment under high renewable penetration [13], data-driven active–reactive dispatch under system uncertainty [14], and distributionally robust optimization (DRO) for resilience against disruptive events [36]. In particular, Du et al. construct an uncertainty set for attack resources and a Wasserstein-metric ambiguity set for their unknown probability distributions in an interdependent power–communication system [36]. This DRO formulation hedges resilience decisions ex ante against distributional ambiguity. By contrast, the present optimization model is a deterministic SOCP on the modeled full-base network and contains neither a scenario set nor a distributional ambiguity set. As detailed in Section 3.4 and Appendix B, its performance under renewable-generation uncertainty is evaluated empirically using three wind/PV forecast-error RMS levels, three independent AR(1) error realizations at each level, and both typical and heavy operating conditions. These 18 combinations are ex post evaluation cases rather than uncertainty scenarios embedded in the optimization problem. The results therefore support the corrective value of rolling feedback within the tested uncertainty range, but do not establish stochastic or distributionally robust guarantees.

This paper therefore proposes, for the coordinated optimization of terminal voltage security and network loss in a multi-station series-coupled renewable energy base, a coordinated active–reactive power optimization method built on a second-order cone relaxation. The method takes the charging and discharging of storage, the wind and PV output, and the reactive power of every source as the decision variables of one global optimization. While tracking the AVC reactive-power command and the active-power delivery schedule, it safeguards terminal voltage security and reduces network loss, and it embeds the model in a model predictive control framework that jointly coordinates the cross-period scheduling of storage and the reactive power of all sources.

2. Materials and Methods

2.1. Structure and Voltage Distribution of the Series-Coupled Wind–PV–Storage Base

A renewable energy base in western China is taken as the example. It consists of two integrated wind–PV–storage stations coupled in series through 220 kV lines. A typical base comprises two step-up stations, each containing a number of wind turbines, PV subarrays, electrochemical storage groups, and SVGs. The wind turbines connect to the 35 kV collector lines as independent nodes and are aggregated to the low-voltage bus of the step-up transformer through several series-connected collector branches; the PV subarrays are aggregated along the collector branches and then connected to the 220 kV section; the

storage is concentrated along the collector branches; and the SVGs are installed on the low-voltage bus side. The 220 kV buses of the two stations are joined by a tie line, and one of them further connects to the grid through a double-circuit long-distance export line. The upper-level dispatch commands are issued to the base on a per-station basis: each station independently receives the reactive-power command $Q_{\mathrm{ref}}^{(s)}(t)$ from the AVC master station and the active-power delivery schedule $P_{\mathrm{ref}}^{\mathrm{demand},(s)}(t)$ from the dispatch center, where s is the station index. The overall wiring topology of the base is shown in Figure 1.

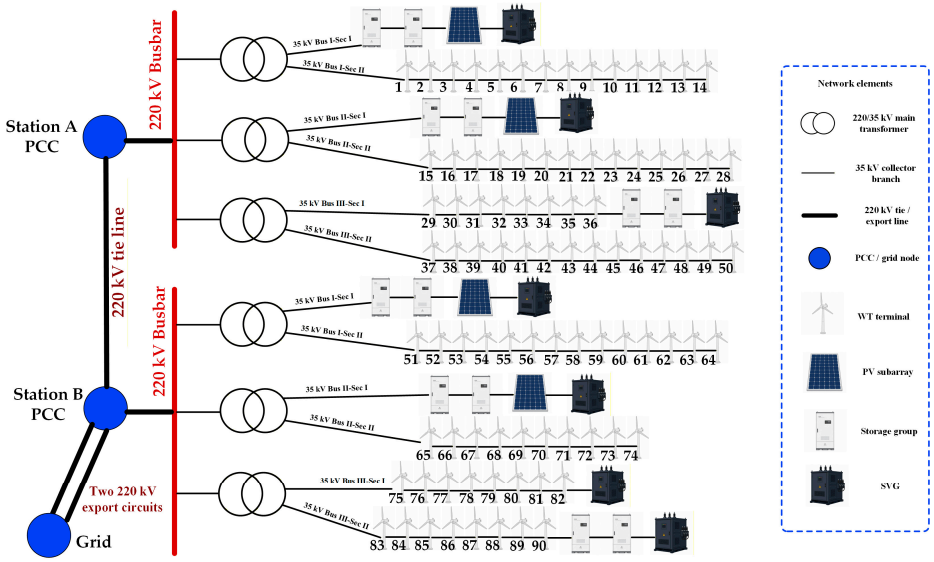


Figure 1. Wiring topology of the two series-coupled stations of the renewable energy base. The labels 1–90 denote the wind-turbine terminal numbers.

2.1.1. Electrical Coupling Between the Two Stations

As Figure 1 shows, the two step-up stations are not mutually independent plants of equal capacity; they form a pronounced electrical coupling at the 220 kV level through the tie line. All power delivered by Station A first flows through the tie line to the 220 kV bus of Station B. It then combines with the output of Station B and enters the grid through the double-circuit export line. This arrangement forms a topology of series aggregation followed by unified delivery. The coupling is quantified below with a linearized DistFlow relation.

Let the voltages of the 220 kV buses of Stations A and B, that is, their respective PCCs, be U_A and U_B; let the grid serve as the slack node with voltage U_0. Let the impedance of tie line A→B be $Z_{\mathrm{tie}} = R_{\mathrm{tie}} + jX_{\mathrm{tie}}$, and let the impedance of the export line B→grid, after equivalent paralleling of the double circuit, be $Z_{\mathrm{send}} = R_{\mathrm{send}} + jX_{\mathrm{send}}$. Let the active and reactive power delivered by the two stations at their respective PCCs be P_A, Q_A and P_B, Q_B. Under the first-order approximation that neglects line charging susceptance and line loss, the active and reactive power on the tie line and on the export line satisfy

$$\begin{cases} P_{\mathrm{tie}} = P_A \\ Q_{\mathrm{tie}} = Q_A \end{cases} \tag{1}$$

$$\begin{cases} P_{\mathrm{send}} = P_A + P_B \\ Q_{\mathrm{send}} = Q_A + Q_B \end{cases} \tag{2}$$

From the linearized DistFlow relation, the 220 kV bus voltage of Station B is

$$U_B \approx U_0 + \frac{(P_A + P_B)R_{\text{send}} + (Q_A + Q_B)X_{\text{send}}}{U_0} \tag{3}$$

Recursing along the tie line to the PCC voltage of Station A gives

$$U_A \approx U_B + \frac{P_A R_{\text{tie}} + Q_A X_{\text{tie}}}{U_B} \tag{4}$$

Combining this with the previous expression yields the explicit dependence of the PCC voltage of Station A on the four-element delivery vector (P_A, Q_A, P_B, Q_B):

$$U_A \approx U_0 + \frac{(P_A + P_B)R_{\text{send}} + (Q_A + Q_B)X_{\text{send}}}{U_0} + \frac{P_A R_{\text{tie}} + Q_A X_{\text{tie}}}{U_B} \tag{5}$$

These relations reveal three kinds of coupling between the two stations.

1. Power-flow coupling: The active and reactive flows on the export line are determined by the sum of the two stations' deliveries, so any power adjustment at one station necessarily acts on the export-corridor current and the corresponding line loss of the other.
2. Voltage coupling: Because $\partial U_A/\partial Q_B = X_{\text{send}}/U_0 > 0$ and $\partial U_A/\partial P_B = R_{\text{send}}/U_0 > 0$, the active and reactive output of Station B directly raises the PCC voltage of Station A and is further conducted to the terminals of Station A through its intra-station collector lines.
3. Reactive-resource coupling: Although the SVGs and storage of the two stations belong to separate stations and each follows its own AVC command, any dispatch action alters the PCC voltage margin of the other station through the relations above, and thereby affects the other station's terminal voltage security and its upper limit of deliverable reactive power.

These couplings indicate that a station optimizing only its own indices, while ignoring its interaction with the other station, may trigger terminal over-voltage at the neighboring station or raise the network-wide loss. This paper therefore merges the two stations into a single DistFlow tree and solves the active and reactive decision variables of all sources jointly on a coupled SOCP model that covers the whole network.

2.1.2. Node Voltage and the Active–Reactive Relationship

Let the PCC voltage of a station be U_{PCC}, let the equivalent voltage of its upstream tie line or export line be U_0 with impedance $Z_0 = R_0 + jX_0$, and let the active and reactive power delivered by the station be P_{out} and Q_{out}. Neglecting the transverse component of the voltage, the PCC voltage can be approximated as

$$U_{\text{PCC}} \approx U_0 + \frac{P_{\text{out}} R_0 + Q_{\text{out}} X_0}{U_0} \tag{6}$$

For the i-th node along an intra-station collector branch, the voltage can be obtained by recursion from the PCC:

$$U_i \approx U_{\text{PCC}} - \sum_{(k,l)\in\mathcal{P}(i)} \frac{P_{kl} R_{kl} + Q_{kl} X_{kl}}{U_{\text{PCC}}} \tag{7}$$

Here $\mathcal{P}(i)$ is the branch path from the PCC to node i; P_{kl} and Q_{kl} are the active and reactive power flows on branch (k, l), and R_{kl} and X_{kl} are its resistance and reactance. Under typical conditions the station delivers positive active power, so along a branch

$P_{kl} < 0$, the flow runs from the end toward the PCC, and the voltage drop is negative; the terminal voltage at the end is therefore higher than the PCC voltage. The larger the reactive output of the station, the more pronounced the rise at the end, and the higher the over-limit risk. Equation (7) further shows that reactive power injected locally by a turbine at the end of a long collector line raises its terminal voltage far more than the same injection by a turbine close to the PCC. This relation is the root of the physical conclusion that follows. Under unified power factor control, every turbine injects reactive power locally at the same power factor, so the reactive injection of the end-of-feeder turbines on a long collector line markedly raises their terminal voltage and causes over-limit. The proposed method, by contrast, jointly optimizes the active and reactive allocation of all turbines under the terminal voltage constraint, so that reactive power is borne more by turbines that have little terminal-raising effect and short transmission paths, while the end-of-feeder turbines deliver less reactive power, thereby holding the terminal voltage within bounds.

2.2. Multi-Source Active–Reactive Joint Dispatch Model

This section presents the complete mathematical model of the multi-source active–reactive joint dispatch of the base, in the order of decision variables, constraints, and objective function; the SOCP convexification form of the model and its rolling multi-period expansion are given afterward.

Let the collector network of the base be represented by the graph $\mathcal{G} = (\mathcal{N}, \mathcal{E})$, which includes the internal networks of the two stations and the tie line. The source set is divided by type into wind turbines $\mathcal{W}$, PV subarrays $\mathcal{V}$, SVGs $\mathcal{S}$, and storage $\mathcal{B}$. In what follows, the active and reactive power of each source is denoted by P and Q with the subscripts w, v, s, b, and the rated apparent capacity by S with the corresponding subscript.

Sign and positive-direction conventions: A unified set of conventions is adopted so that the DistFlow model and the linearized analysis remain symbolically self-consistent.

1. Branch direction: The DistFlow tree is rooted at the grid slack, and a branch $(i,\ j) \in \mathcal{E}$ points from the parent node i to the child node j.
2. Branch flow: $P_{ij},\ Q_{ij}$ are the active and reactive power that flow into the child node j on branch $(i,\ j)$. Under normal operation the base delivers power to the grid, and the flow runs from the end toward the root, so the collector branches commonly satisfy $P_{ij} < 0,\ Q_{ij} < 0$.
3. Node injection: $p_j,\ q_j$ are the sums of the active and reactive power of all sources at node j, with the direction defined so that injection from a source into the collector network is positive; that is, wind and PV output, storage discharge, and SVG capacitive reactive power are positive, whereas storage charging and SVG inductive reactive power are negative. In the DistFlow balance of Equation (14), because the flow is defined from parent to child, the source-positive $p_j,\ q_j$ enter the equation as $-p_j,\ -q_j$, so that for a leaf wind-turbine node $P_{ij} \approx -p_j$, which is consistent with the branch-flow sign above.
4. Capacitive-positive reactive power: The AVC-issued $Q_{\mathrm{ref}}^{(s)}$, the source reactive quantities Q, and the node injection q_j all follow the "capacitive-positive" convention; the reactive power injected by the line-shunt charging susceptance in the π model is likewise capacitive-positive, and in Equation (14) it appears as $-b_j^{\mathrm{sh}} u_j$ with the same sign as $-q_j$.
5. Voltage-squared variable: $u_j = U_j^2 \geq 0$, in per-unit form.

2.2.1. Decision Variables

The model is solved for the entire base over each dispatch period $t \in \mathcal{T}$. The decision variables are grouped into the following six classes by their physical origin.

1. Wind/PV/SVG output: Wind (P_w, Q_w), $w \in \mathcal{W}$; PV (P_v, Q_v), $v \in \mathcal{V}$; SVG reactive power Q_s, $s \in \mathcal{S}$.
2. Storage: Charging power $P_b^{\mathrm{ch}} \geq 0$, discharging power $P_b^{\mathrm{dis}} \geq 0$, reactive power Q_b, and state of charge SOC_b, $b \in \mathcal{B}$; the net discharging power is denoted as $P_b = P_b^{\mathrm{dis}} - P_b^{\mathrm{ch}}$, so as to correctly reflect the asymmetry of the charging and discharging efficiencies.
3. Wind/PV curtailment: $P_n^{\mathrm{curt}}(t) \geq 0$, $n \in \mathcal{W} \cup \mathcal{V}$; the actual grid-connected output after curtailment is $P_n^{\mathrm{act}}(t) = P_n^{\mathrm{MPPT}}(t) - P_n^{\mathrm{curt}}(t)$.
4. Network variables: Branch active and reactive flows P_{ij}, Q_{ij}, squared branch current $l_{ij} = I_{ij}^2$, and squared node voltage $u_i = U_i^2$, with $(i,\ j) \in \mathcal{E}$ and $i \in \mathcal{N}$.
5. Tracking-error slacks: $\xi_P^{(s)},\ \xi_Q^{(s)}$, the deviations of station s in delivered active and reactive power from the dispatch command, $s \in \{A,\ B\}$.
6. Linearization auxiliaries: $q_s^+ \geq 0$ for linearizing $|Q_s|$, and $r_b \geq 0$ for representing the remaining apparent-capacity margin of the storage.

Unlike the conventional practice of treating storage active power P_b as an external input parameter, this paper includes P_b together with P_n^{curt} among the decision variables, so that the active decisions covering storage charging/discharging and wind–PV output are coordinated jointly with the reactive power of all sources within the same convex optimization framework.

2.2.2. Constraints

Wind-turbine capability circle. The reactive capability of a doubly fed induction generator (DFIG) is limited by the rotor-current circle. To preserve the second-order cone structure of the model, the engineering approximation of a fixed stator rated voltage $U_s \approx 1.0$ p.u. is adopted, and U_s in the expression is treated as a constant:

$$P_w^2 + \left(Q_w + \frac{U_s^2}{X_s}\right)^2 \leq \left(\frac{U_s X_m}{X_s} I_{r,\max}\right)^2, \quad w \in \mathcal{W} \tag{8}$$

Here U_s is the stator voltage, X_s and X_m are the stator reactance and the mutual reactance, and $I_{r,\max}$ is the upper limit of the rotor current. With U_s fixed, Equation (8) is a standard second-order cone in the variables $(P_w,\ Q_w)$, corresponding geometrically to a disk whose center is shifted from the origin to $(0, -U_s^2/X_s)$. This approximation mainly affects the boundary location of the DFIG reactive capability and does not change the principal conclusions of this paper regarding the suppression of terminal over-voltage and the spatial reallocation of reactive power; during the Newton–Raphson (NR) validation stage, the terminal voltage constraint is rechecked with the actual node voltages for closed-loop verification. A refined treatment of the voltage-dependent reactive capability curve can take U_s as a variable and preserve convexity through piecewise linearization or a McCormick envelope, which is left to future work. For full-converter wind turbines, the capability circle $P_w^2 + Q_w^2 \leq S_w^2$ is used directly.

PV inverter capability circle:

$$P_v^2 + Q_v^2 \leq S_v^2, \quad v \in \mathcal{V} \tag{9}$$

where S_v is the rated apparent capacity of PV unit v.

SVG regulation range:

$$-Q_{s,\max} \leq Q_s \leq Q_{s,\max}, \quad s \in \mathcal{S} \tag{10}$$

where $Q_{s,\max}$ is the upper limit of the reactive capacity of SVG s.

Storage capability circle. The electrochemical storage provides active and reactive power simultaneously within its capability circle:

$$P_b^2 + Q_b^2 \le S_b^2, \quad b \in \mathcal{B} \tag{11}$$

where S_b is the rated apparent capacity of storage b.

Storage SOC dynamics:

$$SOC_b(\tau+1) = SOC_b(\tau) - \frac{1}{E_{b,\mathrm{cap}}}\left(\frac{P_b^{\mathrm{dis}}(\tau)}{\eta_b^{\mathrm{dis}}} - \eta_b^{\mathrm{ch}} P_b^{\mathrm{ch}}(\tau)\right)\Delta_o,$$

$$SOC_{b,\min} \le SOC_b \le SOC_{b,\max} \tag{12}$$

Here $E_{b,\mathrm{cap}}$ is the storage capacity in MWh, $\Delta_o = 15$ min is the outer MPC step size, $\eta_b^{\mathrm{ch}}, \eta_b^{\mathrm{dis}} \in (0,1]$ are the charging and discharging efficiencies, and $SOC_{b,\min}$ and $SOC_{b,\max}$ are the lower and upper SOC limits, taken here as 0.10 and 0.90. Because simultaneous charging and discharging would increase the two-sided energy loss and raise both the network loss and the objective value, the optimum naturally satisfies $P_b^{\mathrm{ch}} \cdot P_b^{\mathrm{dis}} = 0$ without any complementarity constraint; no simultaneous charging and discharging was observed over the full 96-step case study.

Wind/PV curtailment bound:

$$0 \le P_n^{\mathrm{curt}}(t) \le P_n^{\mathrm{MPPT}}(t), \quad n \in \mathcal{W} \cup \mathcal{V} \tag{13}$$

where $P_n^{\mathrm{MPPT}}(t)$ is the natural output of wind/PV unit n at time t under maximum power point tracking (MPPT).

DistFlow power-flow equations of the full-base coupled tree. The whole network of the base, including the internal networks of the two stations, the tie line, and the export line, is merged into a single radial DistFlow tree, in which the double-circuit export line is combined by parallel equivalence, so that the power flow is described uniformly:

$$\begin{cases} P_{ij} = -p_j + \sum\limits_{k:(j,k)\in\mathcal{E}} P_{jk} + R_{ij} l_{ij} \\ Q_{ij} = -q_j + \sum\limits_{k} Q_{jk} + X_{ij} l_{ij} - b_j^{\mathrm{sh}} u_j \\ u_j = u_i - 2(R_{ij}P_{ij} + X_{ij}Q_{ij}) + (R_{ij}^2 + X_{ij}^2) l_{ij} \\ l_{ij} u_i \ge P_{ij}^2 + Q_{ij}^2 \end{cases} \tag{14}$$

Here R_{ij} and X_{ij} are the resistance and reactance of branch $(i,\ j)$, and b_j^{sh} is the per-unit shunt charging susceptance to ground at node j, corresponding to the equivalent shunt admittance of the 220 kV line π model at the j end. p_j and q_j are the sums of the active and reactive power injected by the sources at node j; they follow the "injection from sources is positive" convention and therefore appear as $-p_j$, $-q_j$ in the DistFlow balance. The reactive power injected by the π-model shunt charging susceptance is capacitive, so $-b_j^{\mathrm{sh}} u_j$ has the same sign as $-q_j$. The last relation in Equation (14), $l_{ij} u_i = P_{ij}^2 + Q_{ij}^2$, is the original nonconvex constraint; it is written directly in the second-order cone relaxed form $l_{ij} u_i \ge P_{ij}^2 + Q_{ij}^2$, and the tightness of the relaxation is verified numerically below. Because the two stations are coupled within the same tree through the tie line, their mutual influence on active and reactive power flow and on terminal voltage is described simultaneously.

Voltage security constraint:

$$u_i^{\min} \le u_i \le u_i^{\max}, \quad \forall i \in \mathcal{N} \tag{15}$$

The 220 kV buses take $u \in \left[0.95^2, 1.05^2\right]$; the turbine terminals and the 35 kV nodes take $u_i \leq 1.068^2$ p.u. The terminal trip threshold is 1.07 p.u., and 1.068 p.u. is adopted inside the SOCP so as to reserve a 0.002 p.u. margin for the SOCP–NR deviation; the measured SOCP–NR deviation of this coupled model is below 0.0005 p.u., so no larger margin is required.

Other constraints. The branch thermal-stability constraint is $l_{ij} \leq I_{ij,\max}^2$, where $I_{ij,\max}$ is the rated current limit of branch (i, j). The grid is taken as the system slack node with voltage U_0, and both the export line and the tie line are included in the DistFlow tree. The PCC voltage of each station is an endogenous variable, determined self-consistently by the combined power flow of the two stations, so no additional voltage-command constraint is imposed.

2.2.3. Objective Function

The objective function comprises five terms: network loss, composite reactive margin, active and reactive delivery tracking error, curtailment penalty, and reactive dispatch cost. Terminal voltage security does not enter the objective; it is guaranteed directly by the node-wise hard voltage constraint of Equation (15).

Objective 1: Network loss.

$$F_1 = \sum_{(i,j)\in\mathcal{E}} R_{ij} l_{ij} \tag{16}$$

Here, $\mathcal{E}$ denotes all modeled series branches retained in the full-base DistFlow tree, including the internal networks of both stations, the 220 kV tie line, and the parallel-equivalent export corridor. In the original DistFlow model, $l_{ij} = \left|I_{ij}\right|^2$ is the squared current magnitude of branch (i,j); therefore, $R_{ij} l_{ij} = R_{ij}\left|I_{ij}\right|^2$ is the active-power loss of that branch in p.u., and Equation (16) gives the total modeled-network active-power loss for one period. In the SOCP relaxation, l_{ij} is retained as the squared-current auxiliary variable and is linked to the branch power flow and sending-end squared voltage by Equation (14); the numerical tightness verification supports recovery of the physical squared-current relation in the reported cases. In the rolling multi-period formulation, these per-period active-power-loss terms are summed over the prediction horizon, and no time-step factor Δ_o is included in this optimization term.

Objective 2: Composite reactive margin. Using the auxiliary variables introduced earlier, namely q_s^+ (which satisfies $q_s^+ \geq Q_s$ and $q_s^+ \geq -Q_s$, linearizing $|Q_s|$) and r_b (which satisfies the second-order cone constraint $(P_b, Q_b, S_b - r_b) \in \mathrm{SOC}$, i.e., $\sqrt{P_b^2 + Q_b^2} + r_b \leq S_b$), the composite reactive margin is defined as

$$F_2 = -\left(\alpha_S \frac{1}{|\mathcal{S}|}\sum_s \frac{Q_{s,\max} - q_s^+}{Q_{s,\max}} + \alpha_B \frac{1}{|\mathcal{B}|}\sum_b \frac{r_b}{S_b}\right) \tag{17}$$

where α_S and α_B are the weighting coefficients of the SVG and storage margin terms. Minimizing F_2 is equivalent to maximizing the sum of the two normalized margins.

Objective 3: Active and reactive delivery tracking error of each station. Let the active and reactive power delivered by station s be $P_{\mathrm{out}}^{(s)}(t)$ and $Q_{\mathrm{out}}^{(s)}(t)$, both metered on the high-voltage side of that station's main transformer; the tracking error is given by the slack variables introduced earlier:

$$\begin{cases} P_{\mathrm{out}}^{(s)} - P_{\mathrm{ref}}^{\mathrm{demand},(s)} = \xi_P^{(s)} \\ Q_{\mathrm{out}}^{(s)} - Q_{\mathrm{ref}}^{(s)} = \xi_Q^{(s)} \end{cases} \tag{18}$$

The tracking objective takes the sum of squares of the slack variables:

$$F_3 = \sum_s \left(w_P \sum_t \xi_P^{(s)2}(t) + w_Q \sum_t \xi_Q^{(s)2}(t) \right) \tag{19}$$

Large weights w_P and w_Q are used to approximate, in a soft-constraint manner, a hard tracking of each station's active-power schedule and reactive-power command. The reactive power is tracked softly: when the reactive command is unreachable under the hard terminal voltage constraint, Q_{out} is allowed to deviate moderately from the command so as to give priority to terminal safety. Each station tracks its own command and is metered on its own 220 kV bus, consistent with the actual operating mode in which the AVC issues commands to each step-up station separately.

Objective 4: Curtailment penalty.

$$F_4 = w_{\text{curt}} \sum_t \sum_{n \in \mathcal{W} \cup \mathcal{V}} P_n^{\text{curt}}(t) \tag{20}$$

where w_{curt} is the unit penalty weight of curtailment, and the summation runs over all time steps and all wind and PV units.

Objective 5: Economic cost of multiple reactive sources. To reflect the actual dispatch cost of each kind of reactive source and to embody the principle of "renewable reactive power first," a unit cost is imposed on the reactive dispatch of each reactive source; the reactive power of the wind and PV units carries no cost and serves as the priority source:

$$F_5 = \sum_t \left(c_S \sum_{s \in \mathcal{S}} |Q_s(t)| + c_B \sum_{b \in \mathcal{B}} |Q_b(t)| \right) \tag{21}$$

where c_S and c_B are the unit reactive-regulation costs of the SVG and the storage, taken as 0.70 CNY/Mvar for the SVG and 0.41 CNY/Mvar for the storage with reference to typical values in the literature; the synchronous condenser does not participate in the reactive regulation of this model and is therefore not counted.

Composite objective:

$$\min F = w_1 F_1 + w_2 F_2 + F_3 + F_4 + F_5 \tag{22}$$

where F_1 takes a large weight, driving l_{ij} toward $(P_{ij}^2 + Q_{ij}^2)/u_i$ at the optimum.

The objective coefficients were selected through hierarchical calibration rather than treated as interchangeable economic parameters because the objective components have different physical scales and operational roles. Voltage, current, device-capability, and SOC limits are directly enforced as hard constraints and are therefore not exchanged through objective weights. The active- and reactive-power tracking coefficients are assigned the highest soft priority to maintain the station-level dispatch commands while allowing deviations when a hard safety constraint becomes active. The network-loss and curtailment coefficients determine the principal soft trade-off between reducing modeled network losses and preserving renewable energy. The reactive-margin and reactive-source-cost terms provide secondary discrimination among feasible solutions that already satisfy the safety and tracking requirements. The high-voltage-branch regularization coefficient is used primarily to maintain numerical tightness. Accordingly, the coefficients reported in Table A2 constitute a calibrated reference setting that balances command tracking, network-loss reduction, renewable-energy utilization, and numerical stability.

To evaluate the robustness of this selection, a one-at-a-time sensitivity analysis was conducted by scaling five practically relevant coefficient groups to 0.5, 1.0, and 2.0 times

their reference values under typical and heavy evening-peak operating conditions. The results identify command tracking and the loss–curtailment balance as the dominant sensitivities, while the reactive-source-cost and high-voltage-regularization terms provide operating-condition-dependent refinement. The complete methodology and quantitative results are presented in Appendix C and Figure A2.

2.3. SOCP Relaxation Solution and Rolling Multi-Period MPC

This section presents the convexified solution form of the foregoing multi-source active–reactive joint dispatch model, in the order of the single-period SOCP standard form and relaxation tightness, followed by the rolling multi-period MPC expansion.

2.3.1. Single-Period SOCP Standard Form and Relaxation Tightness

SOCP standard form. Equation (17) has already been written explicitly through the auxiliary variables q_s^+ and r_b in the standard form of a linear objective plus SOC constraints; the absolute value $|Q|$ in Equation (21) is likewise linearized through $q^+ \geq 0$, $q^+ \geq Q$, $q^+ \geq -Q$; and the squared tracking error ξ^2 in Equation (19) is converted into a convex objective through the rotated second-order cone $(\xi, \sigma, 1) \in \mathrm{SOC}_{\mathrm{rot}}$. Taken together, the objective of Equations (16)–(22) and the full set of constraints of Equations (8)–(15) constitute a standard second-order cone program, which can be automatically transformed by CVXPY and solved by the CLARABEL solver.

Relaxation tightness and numerical validation. The second-order cone relaxation $l_{ij}u_i \geq P_{ij}^2 + Q_{ij}^2$ in Equation (14) is the only source of approximation of the model relative to the original nonconvex AC OPF. The theoretical result that the SOCP relaxation is exact for radial networks under standard conditions can be found in [24,25]; this paper does not rely on that theoretical guarantee as its sole argument, but further confirms the relaxation tightness through the numerical validation of the case study. Specifically, the relaxation gap of branch $(i,\ j)$ at period t is defined as

$$\epsilon_{ij,t} = l_{ij,t}u_{i,t} - (P_{ij,t}^2 + Q_{ij,t}^2) \geq 0 \tag{23}$$

Its maximum and mean over the 96 steps are tabulated separately for the 35 kV collector branches and the 220 kV tie/export lines.

Treatment of high-voltage branch relaxation degeneracy. The base contains 220 kV tie and export lines whose per-unit resistance is extremely small; under the operating condition that combines reverse power flow with the terminal voltage upper limit, such branches may exhibit relaxation degeneracy, in which l_{ij} departs from the cone lower bound. For the branches $\mathcal{E}_{\mathrm{HV}} \subset \mathcal{E}$ whose two ends are both 220 kV nodes, a small current regularization term $\lambda \sum_{(i,j)\in\mathcal{E}_{\mathrm{HV}}} l_{ij}$ is imposed, where λ is taken as about 10 times w_1, to pull the relaxation gap back to the cone lower bound. This regularization acts only on the extremely low-impedance high-voltage corridors, and its bias on the 35 kV collector branches and on the (P, Q) decisions of each source at the optimum is numerically negligible.

2.3.2. Rolling Multi-Period SOCP-MPC

Let the multi-period set be $\mathcal{T}$, the outer step size $\Delta_o = 15$ min, and the number of prediction steps N. A set of SOCP variables is replicated for each period, and the cross-period storage SOC coupling of Equation (12) together with a terminal SOC constraint is imposed. Each AVC cycle is solved on the basis of the N-step-ahead prediction, only the first step is executed, and after the SOC is advanced the problem is re-solved on a rolling basis. The SOC coupling is linear and does not break the second-order cone structure, so the multi-period problem remains a standard SOCP that can be solved online by open-source solvers such as CLARABEL.

In summary, the overall control structure of the proposed method is as follows: each station of the base receives the AVC reactive-power command and the active-power delivery schedule, and feeds them, together with the wind–PV forecast and the SOC measurement, into the full-base coupled SOCP-MPC coordination optimizer; after solving, the active, reactive, and curtailment commands of each source are issued, and the terminal voltage and network loss are evaluated by power flow and fed back, forming a rolling closed loop. The resulting rolling SOCP–MPC procedure is summarized in Figure 2.

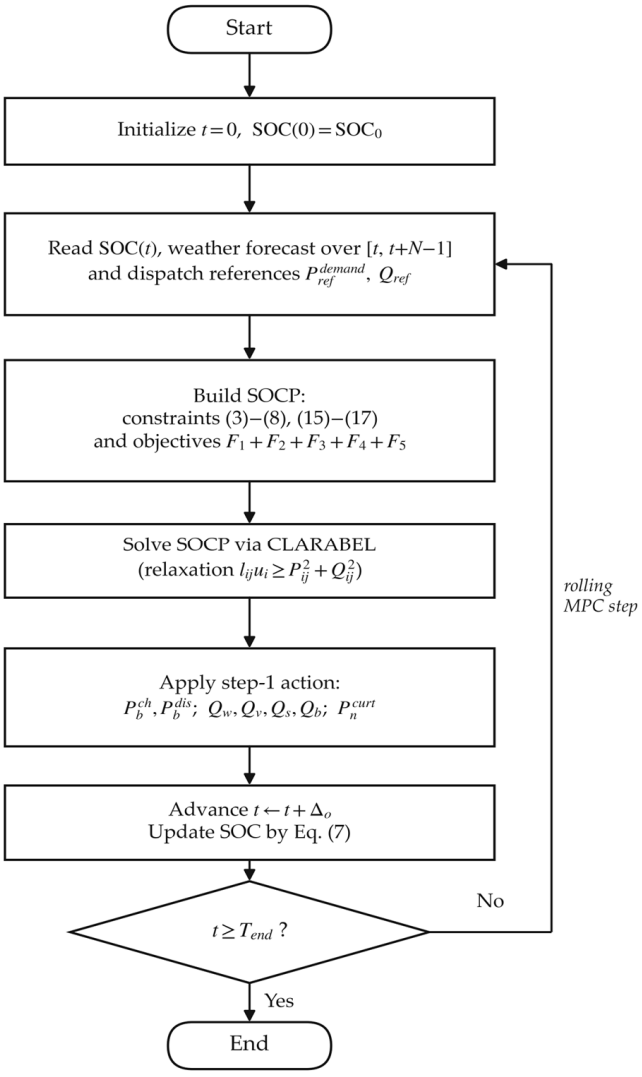


Figure 2. Flowchart of the rolling multi-period SOCP-MPC algorithm.

3. Results

3.1. Test System and Parameters

A full-network simulation model is built on the actual wiring of the two real stations coupled in series through 220 kV, as shown in Figure 1. The main parameters are given below, with detailed data in Appendix A.

Station A: 50 wind turbines with a total installed capacity of 555 MW, distributed over 25 collector branches at 35 kV; PV 200 MWp; storage 150 MW/600 MWh in 6 groups; SVG 150 Mvar in three 50 Mvar units on the 35 kV bus sections. Station B: 40 wind turbines with a total installed capacity of 445 MW, distributed over 20 collector branches; PV 300 MWp; storage 150 MW/600 MWh in 6 groups; SVG 200 Mvar in four 50 Mvar units. The two

stations together have 90 wind turbines, 500 MWp of PV aggregated into four subarrays, 300 MW/1200 MWh of storage in 12 groups, and 350 Mvar of SVG in seven 50 Mvar units.

Coupling and delivery. Station A connects to the 220 kV bus of Station B through a tie line of about 4.9 km; Station B then feeds the grid through an export line of about 21 km in two parallel circuits, with the grid taken as the system slack node. The power of both stations is aggregated and delivered through Station B, forming the series-coupled structure. The turbines of a desert-and-Gobi base are widely spaced and the collector lines are relatively long, so the collector lines in this paper are modeled by their geometric length. The main transformer takes its nominal turns ratio and does not participate in voltage regulation, because the AVC uses a reactive-power command rather than a voltage command; the grid voltage is taken as 1.0 p.u. The whole network has 117 nodes; the two stations together with the tie line and the export line are merged into a single radial DistFlow tree, in which the double-circuit export line is treated as a parallel equivalent, and both the SOCP and the NR validation are based on this full-network topology.

The simulation covers one typical day in 96 steps with a single step size of 15 min. After station-level spatial aggregation and smoothing of the synthetic-day data, the wind output ratio is about 0.16–0.90 and the PV ratio about 0–0.99; the active-power delivery schedule $P_{\mathrm{ref}}^{\mathrm{demand}}$ of each station takes a morning-and-evening double-peak shape with a midday trough; the reactive-power command Q_{ref} is decoupled from the active power and is set at two levels, typical and heavy. The model is constructed in Python/CVXPY 1.4, and the SOCP part is solved by the open-source solver CLARABEL 0.6; the AC power-flow validation is based on the same 117-node Newton–Raphson (NR) program, which shares the topology, impedances, and transformer parameters with the SOCP. Of the 117 nodes, 90 are turbine terminals and the remaining 27 are 35 kV collector nodes, 220 kV buses, and the grid slack node.

SOCP relaxation tightness and NR validation. The SOCP solution of the proposed method is substituted as a given injection into the NR power-flow model and solved step by step, and the branch relaxation gap $\epsilon_{ij,t}$ defined above is computed. The key errors over the 96 steps are summarized in Table 1: the maximum deviation of the network-wide node voltage is below 5×10^{-4} p.u. and the mean deviation is on the order of 10^{-4} p.u.; the maximum relaxation gap of both subsets, the 35 kV collector branches and the 220 kV high-voltage corridors, is below 10^{-3}, and no case occurred in which the SOCP solution was infeasible under the NR model. The numerical results indicate that, within the two operating conditions and parameter ranges studied here, the SOCP relaxation remains tight, and the obtained solution can serve as a high-accuracy feasible solution of the original nonconvex power-flow model; its maximum voltage deviation from the NR solution, below 5×10^{-4} p.u., is far smaller than the 0.002 p.u. margin reserved by the terminal hard constraint, so the objective–constraint combination is numerically closed on the cases studied.

Table 1. Error statistics of the SOCP solution against the NR power-flow validation.

Error Metric	Maximum	Mean
Terminal voltage deviation, all turbines (p.u.)	$<5 \times 10^{-4}$	$\sim 1 \times 10^{-4}$
35 kV node voltage deviation (p.u.)	$<5 \times 10^{-4}$	$\sim 1 \times 10^{-4}$
220 kV bus voltage deviation (p.u.)	$<2 \times 10^{-4}$	$<1 \times 10^{-4}$
35 kV collector-branch relaxation gap $\epsilon_{ij,t}$	$<1 \times 10^{-3}$	$<1 \times 10^{-5}$
220 kV high-voltage-branch relaxation gap $\epsilon_{ij,t}$	$<1 \times 10^{-3}$	$<1 \times 10^{-5}$
Station delivered active-power error (MW)	<0.5	<0.1
Station delivered reactive-power error (Mvar)	<0.3	<0.1

The terminal voltage takes 1.07 p.u. as the typical setting of the turbine high-voltage protection, hereafter called the "trip threshold," and a "terminal over-voltage instance" denotes a turbine–time sample in the simulation whose terminal voltage exceeds 1.07 p.u. This index quantifies the number of samples for which a turbine enters the high-voltage protection risk zone. The compliance rate of the 90 turbine terminals over the 96 steps is the fraction of samples that satisfy $U_{\text{term}} \leq 1.07$ p.u. Two different control strategies are applied to the renewable energy base: the coordinated active–reactive optimal control method proposed in this paper, and the unified power factor control method commonly used in engineering.

3.2. Typical Condition

3.2.1. Command Tracking Accuracy

As Figure 3 shows, the active and reactive curves of the proposed method almost coincide with the black dashed command line over all 96 steps, and the tracking accuracy is at an engineering-negligible level. The curve of unified power factor control follows the command at most instants, but shows a visible active-power deviation during periods of wind–PV surplus or under-delivery, its active-power tracking accuracy being about one order of magnitude lower than that of the proposed method. Both methods can closely track the same reactive command. The real difference between the two methods lies in the terminal voltage and network-loss cost paid to track the same reactive command, which is developed in the following subsections.

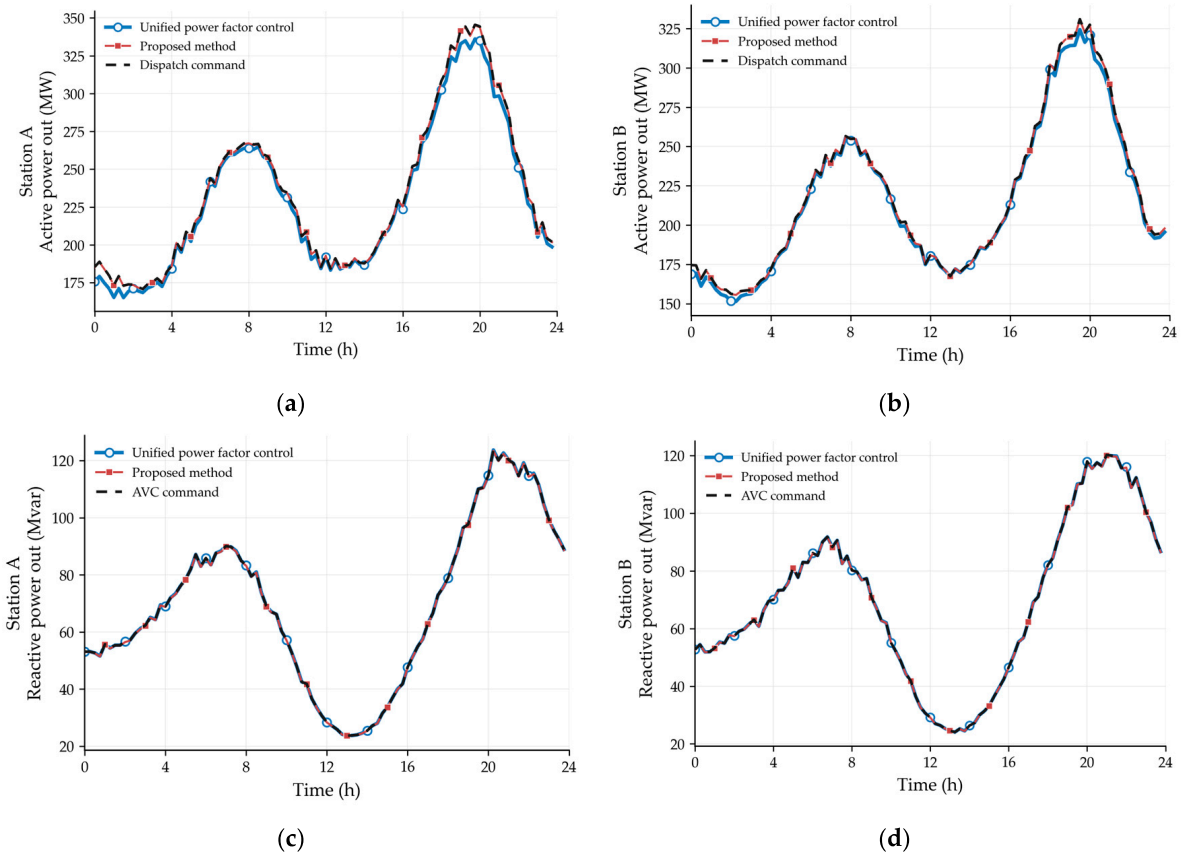
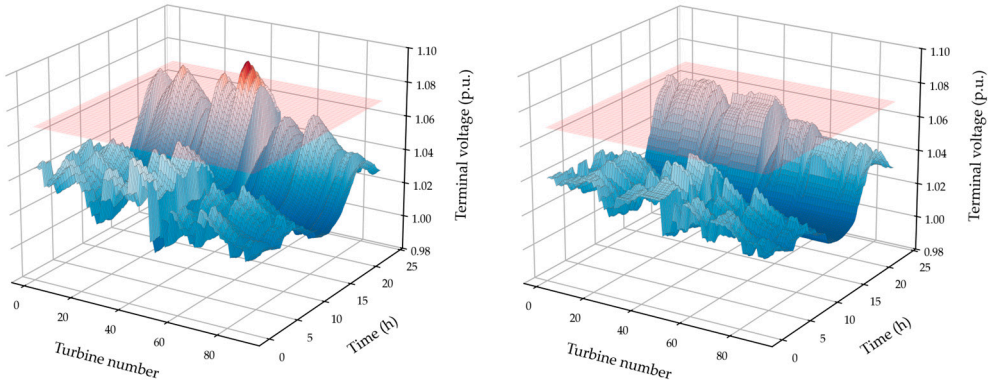


Figure 3. Delivery tracking curves of each station under the typical condition: (**a**) active power of Station A; (**b**) active power of Station B; (**c**) reactive power of Station A; (**d**) reactive power of Station B. In each panel, the blue, red, and black dashed lines denote unified power factor control, the proposed method, and the dispatch/AVC command, respectively.

3.2.2. Capability of the Coordinated Control to Govern Terminal Voltage

As Figure 4a shows, under unified power factor control, the terminal voltage of the whole base forms several local spikes along the time–turbine directions, some of which have already broken through the semi-transparent 1.07 p.u. reference plane, corresponding to the 157 terminal over-voltage instances in Table 2. In Figure 4b the surface of the proposed method is much flatter overall: every terminal voltage stays below the reference plane for the whole horizon, with a peak of only 1.068 p.u. This comparison shows that the proposed method jointly optimizes the reactive outputs of the modeled WT, PV, SVG, and storage resources while tracking the same reactive-power command. Resources whose outputs have a smaller effect on terminal-voltage rise therefore provide a larger share of the required reactive power. This spatial allocation avoids the local terminal over-voltage observed under unified power factor control. Under that baseline, renewable units inject reactive power locally at the same power factor, thereby increasing the voltages of end-of-feeder WT terminals along long collector lines.



(**a**) (**b**)

Figure 4. Terminal voltage of all 90 wind turbines over time under the typical condition: (**a**) unified power factor control; (**b**) the proposed method. The semi-transparent red plane marks the 1.07 p.u. trip threshold. On the surface plots, blue-to-red shading denotes increasing terminal-voltage magnitude.

As Figure 5 shows, the hourly maximum terminal voltage of unified power factor control closely approaches or crosses the 1.07 p.u. red dashed line at several instants, consistent with the 157 over-voltage instances in Table 2. The bars of the proposed method stay below the threshold throughout the 24 h, leaving a safety margin of more than 0.002 p.u. to the threshold. This margin is consistent with the 1.068^2 p.u. terminal hard constraint set in the model, verifying from the external-characteristic side the rationality of the hard constraint and the reserved SOCP–NR deviation.

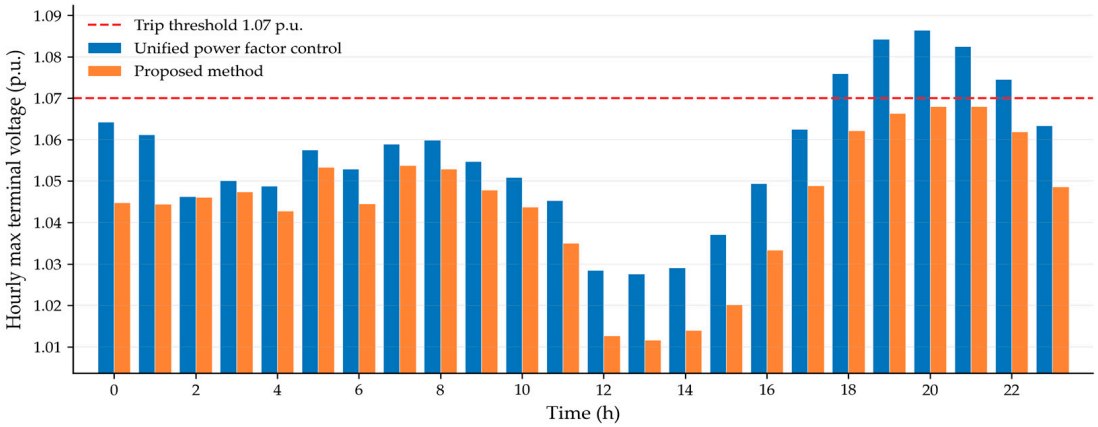


Figure 5. Hourly maximum terminal voltage under the typical condition.

Table 2. Key metrics under the typical condition; the statistics aggregate the terminals of all 90 wind turbines of the base over all time steps.

Scheme	Terminal Compliance @1.07	Over-Voltage Instances (>1.07)	Terminal Max (p.u.)	Total Network Loss (MWh)
Unified power factor control	98.2%	157	1.086	156.8
Proposed method	**100%**	**0**	**1.068**	**136.5**

Note: Bold values indicate the results obtained with the proposed method.

3.2.3. Capability of the Coordinated Control to Optimize Network Loss

As Figure 6 shows, the red curve of the proposed method lies below the blue baseline of unified power factor control during most periods, and the green fill between the two corresponds to the instantaneous loss reduction of the proposed method relative to the baseline; the cumulative result is a 14.1% reduction in the network loss per delivered energy, with the absolute 24 h loss reduced by 13.0%. The physical source of the loss reduction is the spatial optimization of renewable reactive power: instead of distributing reactive power proportionally and uniformly among the turbines along the long collector lines as unified power factor control does, the proposed method lets reactive power be borne more by units close to the PCC with short transmission paths, thereby shortening the average transmission path of reactive power in the collector network and markedly lowering the I^2R loss along the long collector lines.

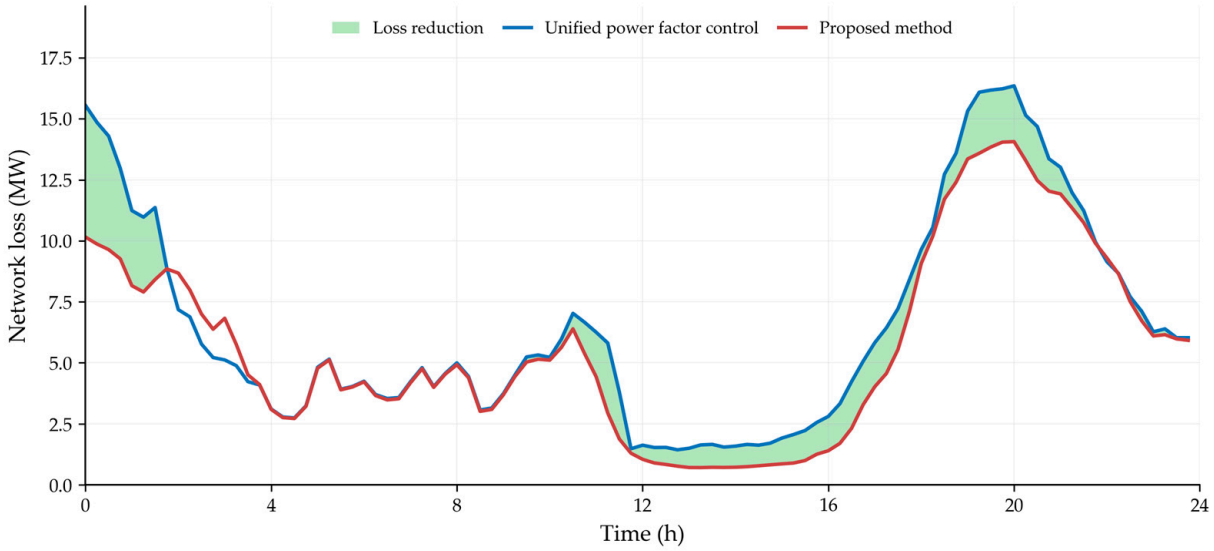


Figure 6. Time-series network loss of the base under the typical condition.

3.3. Heavy Condition (Q_{ref} Evening Peak About 155 Mvar/Station)

3.3.1. Command Tracking Accuracy

Figure 7 gives the active and reactive tracking curves under the heavy condition, whose overall shape is highly similar to that of Figure 3: the curve of the proposed method almost coincides with the command over all 96 steps, whereas the curve of unified power factor control shows a visible active-power deviation during periods of wind–PV surplus or under-delivery. Both methods can closely track the same reactive command.

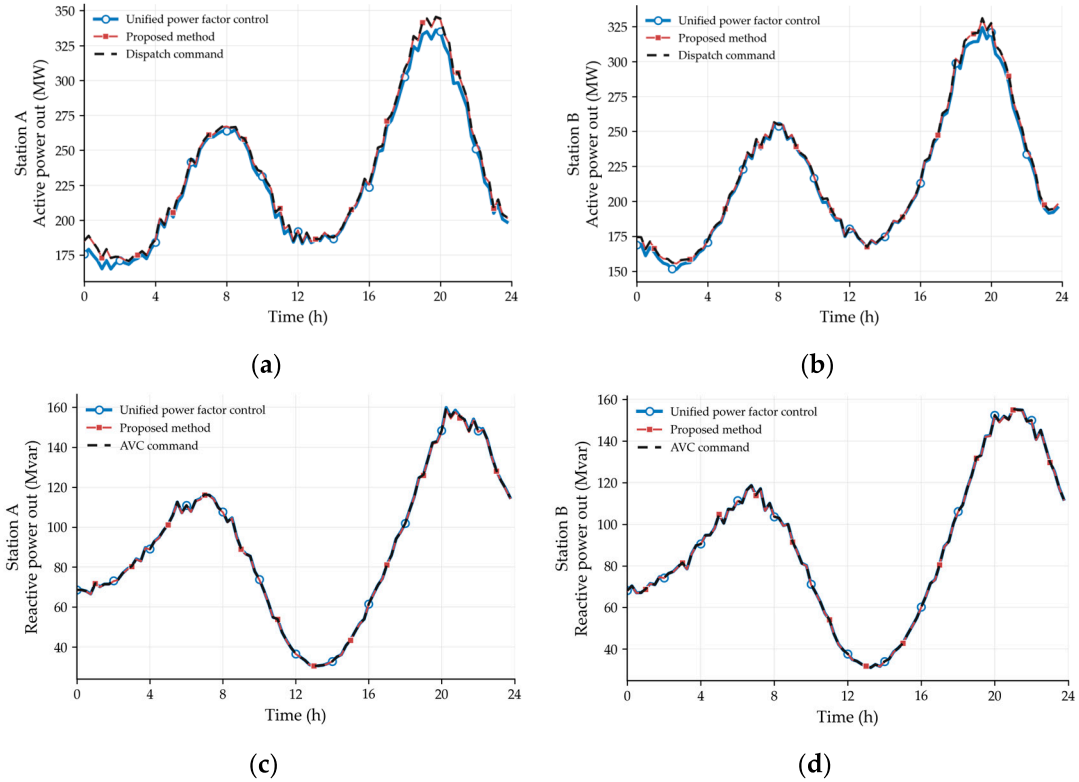


Figure 7. Active and reactive delivery tracking curves of each station under the heavy condition: (**a**) active power of Station A; (**b**) active power of Station B; (**c**) reactive power of Station A; (**d**) reactive power of Station B. Line styles are the same as in Figure 3.

3.3.2. Capability of the Coordinated Control to Govern Terminal Voltage

In Figure 8a the surface under unified power factor control shows a large area of red spikes breaking through the 1.07 p.u. reference plane, corresponding to the 479 over-voltage instances in Table 3 with a peak as high as 1.098 p.u. In Figure 8b the surface of the proposed method still lies entirely below the reference plane, with an upper limit of only 1.068 p.u. Compared with the typical-condition comparison in Figure 4, the over-limit area of the baseline under the heavy condition expands from scattered points to broad bands, and its severity is magnified several-fold; the proposed method, by contrast, still maintains a violation-free state over the whole horizon after the command level is markedly raised, indicating that the convex SOCP framework has a robust capability to constrain terminal voltage under both reactive conditions tested.

Table 3. Daily energy balance and network loss of the base under the heavy and typical conditions.

Quantity (MWh)	Baseline (Heavy)	Proposed (Heavy)	Baseline (Typical)	Proposed (Typical)
Available wind–PV energy (MPPT)	14,764	14,764	14,764	14,764
Curtailed energy	3400	3333	3400	3282
Utilized wind–PV energy	11,365	11,431	11,365	11,483
Grid-side storage net charge	499	449	499	499
Delivered energy	10,708	10,847	10,709	10,847
Daily network loss	157.8	135.4	156.8	136.5
Loss per delivered energy (%)	1.474	1.248	1.464	1.258

As Figure 9 shows, the hourly maximum voltage of unified power factor control clearly crosses the 1.07 p.u. threshold at several instants around the evening peak, corroborating

both the 479 over-voltage instances in Table 3 and the red spike band in Figure 8a. The bars of the proposed method are stably held near 1.068 p.u. over the 24 h, exactly as in Figure 5 for the typical condition. The comparison of the two bar charts shows that, under both the moderate and heavy reactive conditions tested, the proposed method maintains a robust capability to constrain terminal voltage.

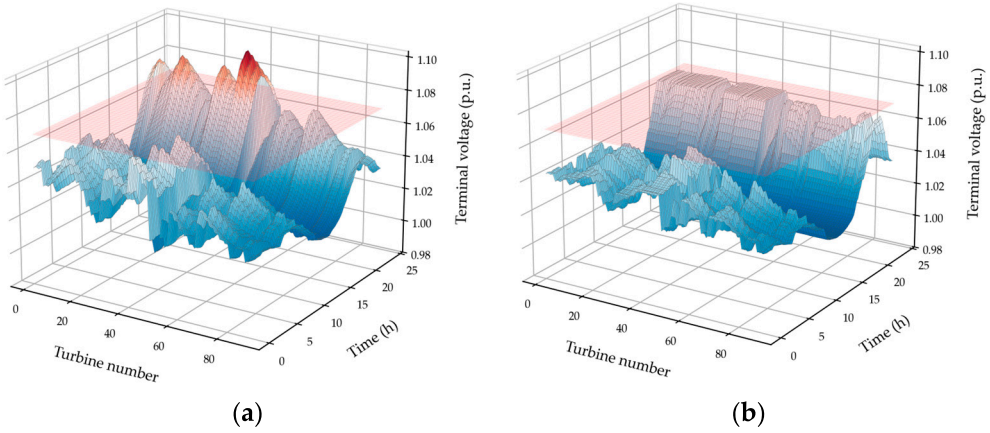


Figure 8. Terminal voltage of all 90 wind turbines over time under the heavy condition: (**a**) unified power factor control; (**b**) the proposed method. The semi-transparent red plane marks the 1.07 p.u. trip threshold. On the surface plots, blue-to-red shading denotes increasing terminal-voltage magnitude.

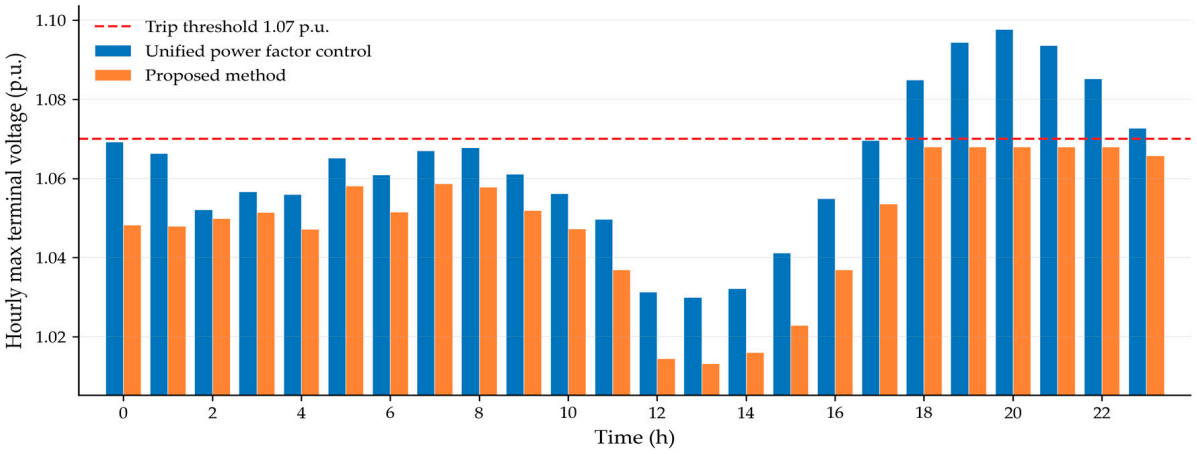


Figure 9. Hourly maximum terminal voltage under the heavy condition.

3.3.3. Capability of the Coordinated Control to Optimize Network Loss

It should be noted that the time-series network loss of the proposed method in Figure 10 approaches or slightly exceeds the baseline during the wind–PV surplus periods from evening to late night. Step-by-step diagnosis shows that these differences arise from the different ways the two methods dispose of surplus power: the baseline directly curtails the excess wind and PV, the curtailed power does not flow through the collector network, and the network loss of that step is therefore lower, at the cost of wind curtailment and insufficient active delivery; the proposed method, by contrast, avoids curtailment as far as possible and charges the surplus into storage for later delivery, so that the charging power flows through the collector lines and the I^2R loss of that step is correspondingly higher. The proposed method trades the instantaneous high loss of a few surplus steps for less curtailment and more accommodation over the whole day; the local time-series crossings are therefore an expected and reasonable phenomenon.

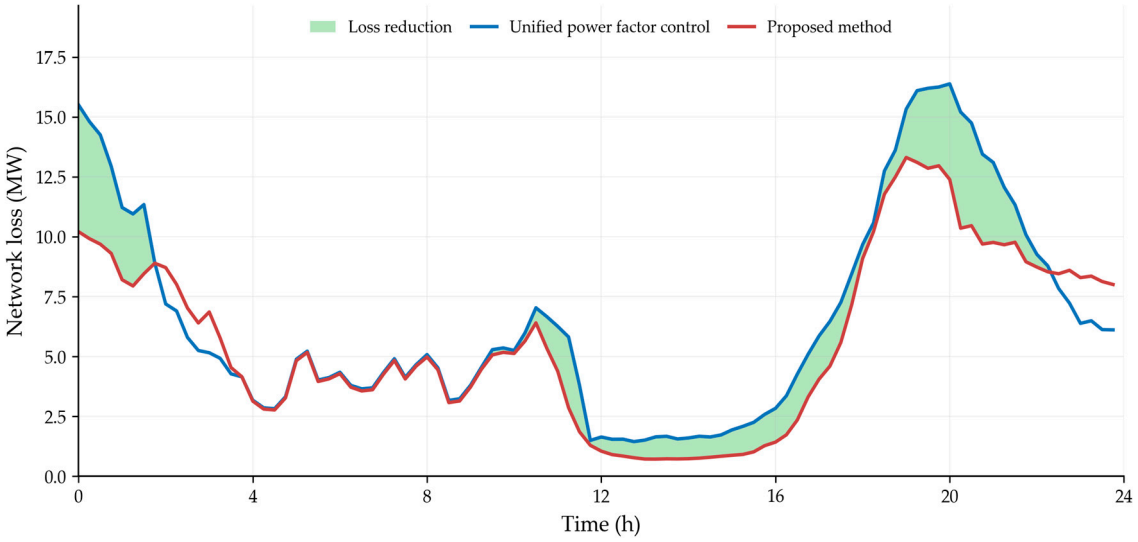


Figure 10. Time-series network loss of the base under the heavy condition.

Because the two methods deliver, curtail, and pass different amounts of energy through the network, the network loss is assessed on the full-day energy balance and normalized by the delivered energy, as summarized in Table 3.

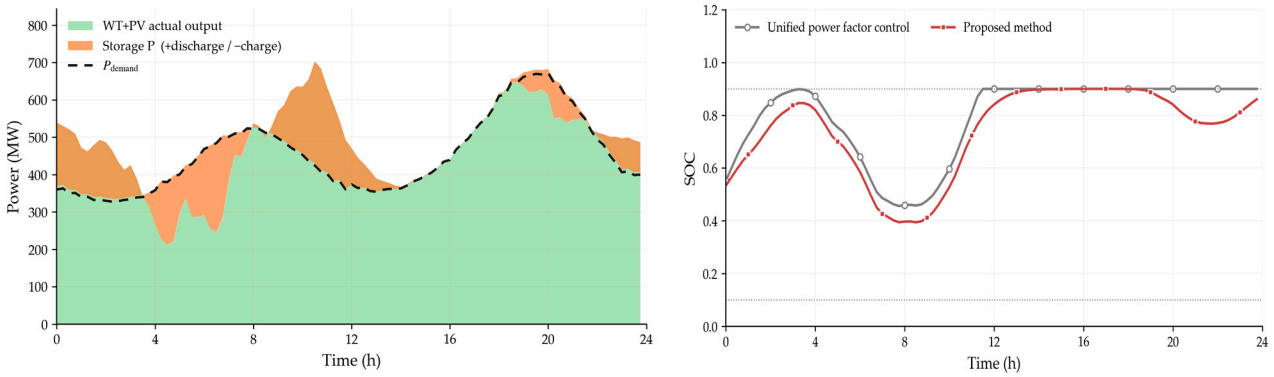
As Table 3 shows, under both conditions the proposed method delivers more energy and curtails less wind and PV than unified power factor control, and by accommodating more renewable energy it passes more energy through the collector network. Even so, its loss per delivered energy falls from 1.474% to 1.248% under the heavy condition and from 1.464% to 1.258% under the typical condition, a normalized reduction of 15.3% and 14.1%, respectively. The absolute daily network loss falls by 14.2% under the heavy condition and by 13.0% under the typical condition.

As in the typical condition, this reduction arises from the spatial reallocation of renewable reactive power: reactive power is borne more by units close to the PCC with short transmission paths, which shortens the average reactive transmission path in the collector network and lowers the I^2R loss along the long collector lines.

3.3.4. Cross-Period Storage Scheduling

Figure 11a shows that the active-power balance over the day exhibits the typical structure of renewable-dominated generation with storage peak-shaving: during the WT+PV surplus periods such as early morning, 4–7 h, and midday, 12–16 h, the storage charges with $P_{\text{stor}} < 0$ to keep the active delivery from exceeding P_{demand}; during the morning and evening peaks, 7–10 h and 16–22 h, when WT+PV cannot match P_{demand}, the storage discharges with $P_{\text{stor}} > 0$ to make up the shortfall; the sum of the green WT+PV output and the orange storage output always closely follows the black dashed P_{demand}, quantitatively confirming the accurate tracking of the active-power delivery schedule by the proposed method. Figure 11b shows that the average SOC trajectories of the two methods are highly consistent in overall shape: starting from an initial value of 0.5, the SOC charges to about 0.88 in the early morning, discharges to a daily minimum of about 0.40 at the morning peak, charges to the 0.90 upper limit at midday, discharges to about 0.75 at the evening peak, and recovers overnight to a final value of about 0.86 under the heavy condition and 0.90 under the typical condition; the storage therefore ends the day with net stored energy instead of returning to its initial 0.5, consistent with the grid-side storage net charge row of Table 3 and reflecting that the available wind–PV energy exceeds the delivery schedule. This trajectory shape reflects that, under the same P_{demand} and SOC limits, the energy-scheduling task of the storage is itself nearly determined. A subtle difference exists between the two

methods: the SOC of the proposed method at the evening peak is about 0.05–0.1 lower than that of the baseline, originating from the different surplus-disposal strategies; that is, the proposed method tracks P_{demand} accurately and absorbs more surplus into storage for delivery during the later high-demand periods, corresponding to the operating feature of less curtailment and more accommodation. The storage reaches the 0.90 upper limit several times and approaches the 0.40 region within the 24 h, indicating that the cross-period SOC constraint is necessary for maintaining the energy boundary of the storage, in agreement with the cross-period coupling and terminal SOC design of Equation (12) in the rolling multi-period MPC framework.



(**a**) (**b**)

Figure 11. Operation of the base under the heavy condition: (**a**) active-power balance, showing WT+PV actual output, storage charging/discharging, and the active-power delivery schedule P_{demand}; (**b**) base-average state of charge of the storage under the two methods. In (**b**), the gray and red curves denote unified power factor control and the proposed method, respectively. In panel (**a**), the black dashed curve denotes the active-power delivery schedule, P_{demand}.

3.3.5. Summary of Key Metrics

Table 4 summarizes the key performance metrics of the two control strategies under the heavy condition.

Table 4. Key metrics under the heavy condition; the statistics aggregate the terminals of all 90 wind turbines of the base over all time steps.

Scheme	Terminal Compliance @1.07	Over-Voltage Instances (>1.07)	Terminal Max (p.u.)	Total Network Loss (MWh)
Unified power factor control	94.5%	479	1.098	157.8
Proposed method	**100%**	**0**	**1.068**	**135.4**

Note: Bold values indicate the results obtained with the proposed method.

3.4. Robustness of the Rolling Closed Loop to Forecast Error

The foregoing case studies use deterministic output. To examine the feedback value of the rolling multi-period framework under uncertainty, a correlated forecast error is injected into the wind and PV output (wind RMS 12%, PV 8%, AR(1)-correlated), and two execution modes are compared on the realized output: an open-loop mode that commits the dispatch computed from the forecast without re-solving, and a closed-loop mode that re-solves on a rolling basis after measuring the realized output at each step and executes only the first step. Both modes look ahead with the forecast only; the aggregate results are listed in Table 5.

As Table 5 shows, on the realized output the open-loop execution suffers a reactive-power mismatch caused by the forecast deviation: under the heavy condition the terminal

voltage exceeds the trip threshold in 27 instances (peak 1.072 p.u.) and the reactive tracking error reaches 11.7 Mvar, while under the typical condition, whose reactive stress is lower, it incurs no over-voltage yet still leaves a 10.2 Mvar tracking error. The rolling closed loop re-solves with the measured output at every step, holding the terminal voltage at 1.068 p.u. with no over-voltage and keeping the reactive tracking error within 1.2 Mvar.

As Figure 12 shows, the open-loop terminal voltage tracks close to the closed loop for most of the day but overshoots the 1.07 p.u. threshold around the evening peak, where the forecast under-predicts the renewable output; the rolling closed loop instead re-solves on the measured output and holds the maximum terminal voltage at 1.068 p.u. throughout.

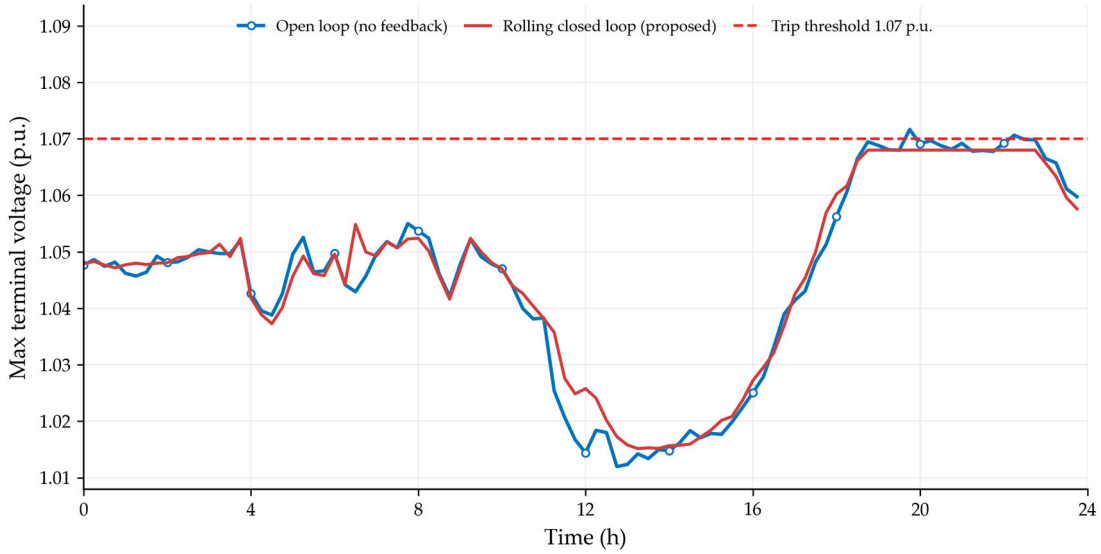


Figure 12. Maximum terminal voltage over time under wind–PV forecast error (heavy condition), for open-loop versus rolling closed-loop execution, with the 1.07 p.u. trip threshold.

As Figure 13 shows, the open-loop reactive tracking error fluctuates strongly with the forecast deviation and reaches about 12 Mvar, whereas the rolling closed loop keeps it close to zero throughout. The value of the rolling closed loop thus lies in terminal voltage security and command-tracking correction under uncertainty, which is precisely the purpose of embedding the present model in a rolling multi-period framework.

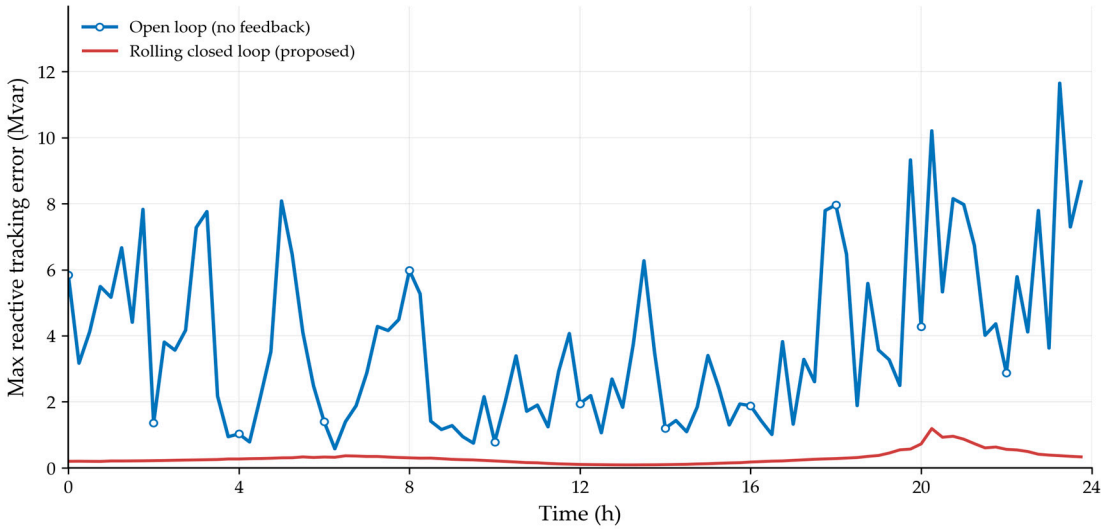


Figure 13. Maximum reactive tracking error over time under wind–PV forecast error (heavy condition), for open-loop versus rolling closed-loop execution.

Table 5. Terminal voltage security and tracking accuracy of open-loop versus rolling closed-loop execution under forecast error (heavy/typical condition).

Execution Mode	Terminal Max (p.u.)	Over-Voltage Instances	Reactive Tracking Error Max (Mvar)
Open loop (no feedback)	1.072/1.068	27/0	11.7/10.2
Rolling closed loop (proposed)	1.068/1.068	0/0	1.2/0.3

3.5. Algorithm Performance

The modeled full-base network contains 117 nodes, including 90 wind-turbine terminals, four aggregated PV subarrays, seven SVGs, and 12 storage resources. At each rolling update, the proposed SOCP-MPC solves a four-period prediction problem corresponding to a 1 h look-ahead horizon and executes only the first control action. Before CVXPY canonicalization, the implemented four-period problem contains 2832 scalar decision variables, 1492 scalar equality constraints, and 3196 scalar inequality constraints. The formulation is a continuous SOCP without integer variables, and the network, device, and operating constraints are organized as repeated per-period blocks coupled through the storage SOC equations.

The computational environment is reported in Table A3. Under the heavy operating condition, five repeated four-period MPC optimizations required 3.70–3.85 s end to end, with an average of 3.80 s and a worst observed value of 3.85 s. The end-to-end time includes model construction, CVXPY canonicalization, and numerical optimization, whereas the solver-reported numerical solution time averaged 0.041 s; the ex post Newton–Raphson validation is performed separately and is not included in this timing. Since the rolling dispatch interval is 15 min (900 s), the worst observed wall time occupies approximately 0.43% of one dispatch cycle, leaving more than a 230-fold computational margin. The proposed framework therefore satisfies the real-time operational requirement of the modeled large-scale two-station renewable energy base.

3.6. Parameter Sensitivity Analysis

A one-at-a-time sensitivity analysis was conducted using the four-period evening high-stress horizon under both the typical and heavy operating conditions. Three groups of parameters were examined while all other network parameters, operating constraints, objective weights, dispatch commands, and initial SOC values were held fixed. First, renewable availability, representing the operational renewable penetration level, was varied by multiplying the available wind/PV power profiles by 0.8, 1.0, and 1.2, subject to their rated-power limits. Second, the storage converter apparent-power rating and energy capacity were simultaneously multiplied by 0.75, 1.0, and 1.25. Third, the modeled terminal-voltage upper limit was set to 1.066, 1.068, and 1.070 p.u. The resulting maximum turbine-terminal voltage, modeled full-base network loss per delivered energy, and renewable curtailment are summarized in Table 6.

All 18 cases returned feasible solutions. Across the complete parameter sweep, the maximum active- and reactive-power tracking errors were 0.530 MW and 0.675 Mvar, respectively; the storage SOC remained within 0.379–0.594; and the maximum conic relaxation residual was 2.28×10^{-6}). Renewable availability was the principal factor affecting renewable curtailment and modeled full-base network loss per delivered energy. Changing the storage rating produced negligible changes in terminal voltage, command tracking, network loss, and curtailment, while increasing the storage capacity narrowed the normalized SOC range from 0.420–0.551 to 0.452–0.530 under the typical condition and from 0.391–0.552 to 0.434–0.531 under the heavy condition. Under the heavy condition, tightening the terminal-voltage upper limit from 1.070 to 1.066 p.u. increased the maximum

reactive-power tracking error from 0.501 to 0.675 Mvar and renewable curtailment from 81.6 to 99.3 MWh, while reducing the loss per delivered energy from 2.569% to 2.459%. These results demonstrate the robustness of the proposed method to variations in renewable availability, storage capacity, and the terminal-voltage limit, while revealing the trade-off among voltage security, command tracking, network loss, and renewable curtailment.

Table 6. One-at-a-time sensitivity results for renewable availability, storage capacity, and the terminal-voltage limit.

Parameter and Tested Values	Maximum Terminal Voltage (p.u.), Typical/Heavy	Loss per Delivered Energy (%), Typical/Heavy	Curtailment (MWh), Typical/Heavy
Renewable-availability factor: 0.8/1.0/1.2	1.0660–1.0664/1.0680	2.251–2.776/2.222–2.690	12.7–167.8/21.8–183.7
Storage apparent-power and energy capacity: 0.75/1.0/1.25	1.06636/1.0680	2.59322–2.59323/ 2.52121–2.52132	approximately 74.566/88.897–88.905
Terminal-voltage upper limit: 1.066/1.068/1.070 p.u.	1.0660–1.0664/ 1.0660–1.0700	2.5932–2.5934/2.459–2.569	74.55–74.57/81.6–99.3

4. Discussion and Conclusions

For two real integrated wind–PV–storage renewable energy stations coupled in series through 220 kV lines, this paper establishes a full-network coupled convex optimization model that jointly considers active and reactive power. The model takes the charging and discharging of storage, the wind and PV output, and the reactive power of all sources as the decision variables of the same SOCP. While tracking the AVC reactive-power command and the active-power delivery schedule of each station, it suppresses the terminal high-voltage risk through node-wise terminal voltage hard constraints and reduces the operating network loss; the model is embedded in a rolling multi-period MPC framework that jointly coordinates the cross-period charging and discharging of storage with the reactive dispatch of all sources. The core physical basis of the proposed method is the law revealed by Equation (7): reactive power injected locally by a turbine at the end of a long collector line raises its terminal voltage far more than injection near the PCC. Instead of distributing reactive power proportionally and uniformly among the turbines as unified power factor control does, the proposed method jointly optimizes the active and reactive allocation of all renewable units, so that reactive power is borne more by units that have little terminal-raising effect and short transmission paths, thereby achieving the two objectives of terminal voltage security and loss reduction at the same time. The case results show that, compared with the unified power factor control baseline, the proposed method tracks the active and reactive delivery commands of each station accurately, keeps the terminal voltage of the whole base below the trip threshold over the whole horizon with no terminal over-voltage instance observed, and reduces the network loss per delivered energy by 14.1% under the typical condition and by 15.3% under the heavy condition; both gains arise from the spatial reallocation of renewable reactive power among the units. Under wind–PV forecast error, the rolling closed loop further maintains terminal voltage security that an open-loop schedule fails to hold. The main conclusions of this paper are as follows.

1. Multi-station coordinated modeling. Different from the single-station equivalent treatment, this paper performs unified coordination on the full-network DistFlow tree of the two stations coupled in series through the tie line, and quantifies three kinds of inter-station coupling, namely power flow, voltage, and reactive resource,

through a linearized relation. A station optimizing only its own indices, while ignoring its interaction with the other station, may trigger terminal over-voltage at the neighboring station or raise the network-wide loss; full-network coupled optimization is therefore, for this kind of topology, not merely a modeling refinement but an engineering necessity.

2. Convex optimization framework of joint active and reactive power. The cross-period charging and discharging of storage, the wind and PV output, and the reactive allocation of all sources are unified as the decision variables of the same SOCP, with the dispatch economy of multiple reactive sources accounted for; numerical validation shows that the SOCP relaxation is well tightened on the system studied here, and after back-substitution into the AC power flow, the recovered operating point is AC-feasible with a relaxation gap below 1×10^{-3}, serving as a high-quality near-optimal solution of the original nonconvex OPF. On an i7-12700/32 GB RAM platform the single-step solving time is about 2–4 s, which is within the minute-level dispatch cycle, so the method has the potential for online application within a minute-level cycle.
3. Effectiveness of the terminal voltage security constraint. Using the terminal compliance rate to quantify how close the terminal voltage is to the trip threshold, the proposed method keeps the terminal voltage of the whole base below 1.068 p.u. under both the typical and heavy conditions, with no terminal over-voltage instance observed; unified power factor control exhibits terminal over-limit under both conditions, with the compliance rate falling to 98.2% and 94.5% and the over-voltage instances numbering 157 and 479, respectively. The physical root lies in the difference in the spatial allocation of reactive power among the turbines: the proposed method jointly optimizes the reactive allocation of all renewable units under the terminal voltage constraint, so that it is borne more by units with little terminal-raising effect; the unified power factor baseline distributes reactive power proportionally and uniformly among the turbines, and the reactive power injected locally by the end-of-feeder turbines on a long collector line raises the terminal voltage markedly.

Author Contributions: Conceptualization, Y.Y., P.Z. and G.Y.; methodology, Y.Y., P.Z. and D.Y.; software, Y.Y., B.N. and D.Y.; validation, Y.Y., P.Z., G.Y. and Z.H.; formal analysis, Y.Y. and G.Y.; investigation, Y.Y. and B.Y.; resources, Y.Y.; data curation, B.N.; writing—original draft preparation, D.Y.; writing—review and editing, Y.Y. and D.Y.; visualization, P.Z.; supervision, Z.H.; project administration, Y.Y.; funding acquisition, Y.Y. All authors have read and agreed to the published version of the manuscript.

Funding: This research was funded by Huadian Electric Power Research Institute Co., Ltd., under the Science and Technology Project "Development of Station Voltage-Support Models and Optimization-Solving Service for Large-Scale Renewable Energy Bases in Xinjiang"; no grant number was assigned.

Data Availability Statement: The data presented in this study are available on request from the corresponding author.

Conflicts of Interest: Authors Yeping Yin, Ping Zhang, Gengning Ying and Bin Niu were employed by Huadian Electric Power Research Institute Co., Ltd. The remaining authors declare that the research was conducted in the absence of any commercial or financial relationships that could be construed as potential conflicts of interest. The authors declare that this study received funding from Huadian Electric Power Research Institute Co., Ltd. The funder was not involved in the study design, collection, analysis, interpretation of data, the writing of this article or the decision to submit it for publication.

Appendix A. Full Parameters of the Two-Station Test System

This appendix gives the complete data of the anonymized test system built from the parameters of a real wind–PV–storage base, for independent reproduction.

Table A1. Installed capacity and topology parameters of the two stations.

Parameter	Station A	Station B
Wind turbines/total capacity	50/555 MW	40/445 MW
Number of collector branches	25	20
PV (MWp)	200	300
Storage P/E	150 MW/600 MWh, 6 groups	150 MW/600 MWh, 6 groups
Storage charge/discharge efficiency $\eta_b^{\mathrm{ch}}/\eta_b^{\mathrm{dis}}$	0.95/0.95	0.95/0.95
Storage SOC lower/upper limits	10%/90%	10%/90%
SVG	3×50 Mvar	4×50 Mvar
Main transformer	3×240 MVA, $u_k = 14\%$	3×240 MVA, $u_k = 14\%$
Main transformer ratio	230/37 kV, fixed	230/37 kV, fixed

220 kV channel. The tie line from Station A to Station B is about 4.9 km, with per-unit-length $r = 0.06\ \Omega$/km, $x = 0.40\ \Omega$/km, and $b = 2.8\ \mu$S/km; the export line from Station B to the grid is about 21 km in two parallel circuits, with the same parameters. The 35 kV collector branches are modeled by the geometric length of each branch, with a length factor of 1.3 to reflect the long collector lines of a desert-and-Gobi base, and per-unit-length $r = 0.27\ \Omega$/km and $x = 0.35\ \Omega$/km. The grid is taken as a fixed slack with $U_0 = 1.0$ p.u., and the model does not include the equivalent impedance or short-circuit capacity of the grid.

Table A2. Composite-objective weights and reactive costs.

Parameter	Value	Unit/Note
w_1 (network loss)	1.0×10^1	per-unit
w_2 (reactive margin)	1.0	per-unit
w_P (active tracking)	2.0×10^4	soft-constraint weight, approximates hard active tracking
w_Q (reactive tracking)	1.0×10^4	soft-constraint weight, yields actively when the terminal hard constraint binds
w_{curt} (curtailment)	1.0×10^3	avoids unnecessary curtailment
c_S (SVG reactive cost)	0.70	CNY/Mvar; representative multi-reactive-source economic value from the literature
c_B (storage reactive cost)	0.41	CNY/Mvar, as above
λ (HV branch regularization)	1.0×10^2	acts only on branches with both ends at 220 kV
$u_{\mathrm{term}}^{\max}$	1.068^2 p.u.	adopted inside the SOCP, reserving a 0.002 p.u. margin for the NR deviation
$u_{220}^{\max/\min}$	$1.05^2/0.95^2$	upper/lower limits of the 220 kV buses

Table A3. Solving and validation environment.

Item	Configuration
Modeling	Python 3.11 + CVXPY 1.4
SOCP solver	CLARABEL 0.6 (open-source; consistency check against MOSEK 10.0 from MOSEK ApS, Copenhagen, Denmark shows an objective-value deviation $< 1 \times 10^{-4}$ on the cases tested)

Table A3. *Cont.*

Item	Configuration
Power-flow validation	Full-network 117-node Newton–Raphson, convergence threshold $\|\Delta \boldsymbol{x}\| < 10^{-6}$
MPC prediction horizon	$N = 4$ (1 h look-ahead), outer step size Δ_o= 15 min
Hardware	Intel Core i7-12700 CPU (Intel Corporation, Santa Clara, CA, USA)/32 GB RAM/Windows 11
Single-step SOCP solving time	2–4 s

Data anonymization note: The topology and installed capacities provided in this appendix originate from an actual project, and the per-unit-length line parameters are anonymized and converted to typical engineering design values; the station names, geographic locations, and operator information have all been anonymized. This test system can be used as a representative case for wind–PV–storage bases of similar scale.

Appendix B. Forecast-Error Sensitivity of the Rolling Closed Loop

To determine whether the uncertainty results depend on a single forecast-error magnitude or realization, an additional sensitivity analysis was conducted using three wind/PV forecast-error RMS levels: 8%/5%, 12%/8%, and 16%/11%, representing mild, baseline, and severe uncertainty, respectively. The AR(1) correlation coefficient was fixed at 0.7. Three independent error realizations were evaluated at each level under both the typical and heavy operating conditions. The network model, constraints, objective weights, dispatch commands, and 96-step simulation horizon were unchanged. The results are summarized in Table A4 and Figure A1.

Table A4. Sensitivity of terminal voltage security and reactive tracking to the forecast-error RMS level. Values are the mean [minimum–maximum] over three independent error realizations.

Condition	Forecast-Error RMS (WT/PV)	Execution Mode	Maximum Terminal Voltage, Mean [Min–Max] (p.u.)	Over-Voltage Instances, Mean [Min–Max]	Maximum Reactive Tracking Error, Mean [Min–Max] (Mvar)
Typical	8%/5%	Open loop (no re-solving)	1.0684 [1.0672–1.0698]	0.0 [0–0]	9.36 [8.59–10.61]
Typical	8%/5%	Rolling closed loop (proposed)	1.0680 [1.0680–1.0680]	0.0 [0–0]	0.34 [0.34–0.34]
Typical	12%/8%	Open loop (no re-solving)	1.0687 [1.0669–1.0708]	1.3 [0–4]	13.26 [10.22–16.48]
Typical	12%/8%	Rolling closed loop (proposed)	1.0680 [1.0680–1.0680]	0.0 [0–0]	0.34 [0.34–0.34]
Typical	16%/11%	Open loop (no re-solving)	1.0693 [1.0674–1.0717]	4.7 [0–14]	18.13 [13.80–22.79]
Typical	16%/11%	Rolling closed loop (proposed)	1.0680 [1.0680–1.0680]	0.0 [0–0]	0.34 [0.34–0.34]
Heavy	8%/5%	Open loop (no re-solving)	1.0708 [1.0705–1.0714]	18.0 [8–33]	9.20 [8.13–10.58]

Table A4. *Cont.*

Condition	Forecast-Error RMS (WT/PV)	Execution Mode	Maximum Terminal Voltage, Mean [Min–Max] (p.u.)	Over-Voltage Instances, Mean [Min–Max]	Maximum Reactive Tracking Error, Mean [Min–Max] (Mvar)
Heavy	8%/5%	Rolling closed loop (proposed)	1.0680 [1.0680–1.0680]	0.0 [0–0]	1.19 [1.18–1.19]
Heavy	12%/8%	Open loop (no re-solving)	1.0721 [1.0717–1.0730]	51.3 [27–93]	13.50 [11.65–16.40]
Heavy	12%/8%	Rolling closed loop (proposed)	1.0680 [1.0680–1.0680]	0.0 [0–0]	1.18 [1.17–1.19]
Heavy	16%/11%	Open loop (no re-solving)	1.0734 [1.0728–1.0744]	78.7 [45–142]	18.51 [15.87–22.65]
Heavy	16%/11%	Rolling closed loop (proposed)	1.0680 [1.0680–1.0680]	0.0 [0–0]	1.17 [1.14–1.19]

An over-voltage instance in Table A4 denotes one terminal–time pair with a voltage above 1.07 p.u. Under the typical condition, the mean maximum reactive tracking error of the open-loop execution increases from 9.36 to 18.13 Mvar as the forecast-error level increases, whereas the corresponding rolling closed-loop value remains approximately 0.34 Mvar. Under the heavy condition, the mean maximum terminal voltage of the open-loop execution increases from 1.0708 to 1.0734 p.u., and its mean maximum reactive tracking error increases from 9.20 to 18.51 Mvar. By contrast, the rolling closed loop maintains the maximum terminal voltage at approximately 1.0680 p.u., produces no terminal over-voltage instance, and keeps the maximum reactive tracking error within 1.19 Mvar over all tested realizations.

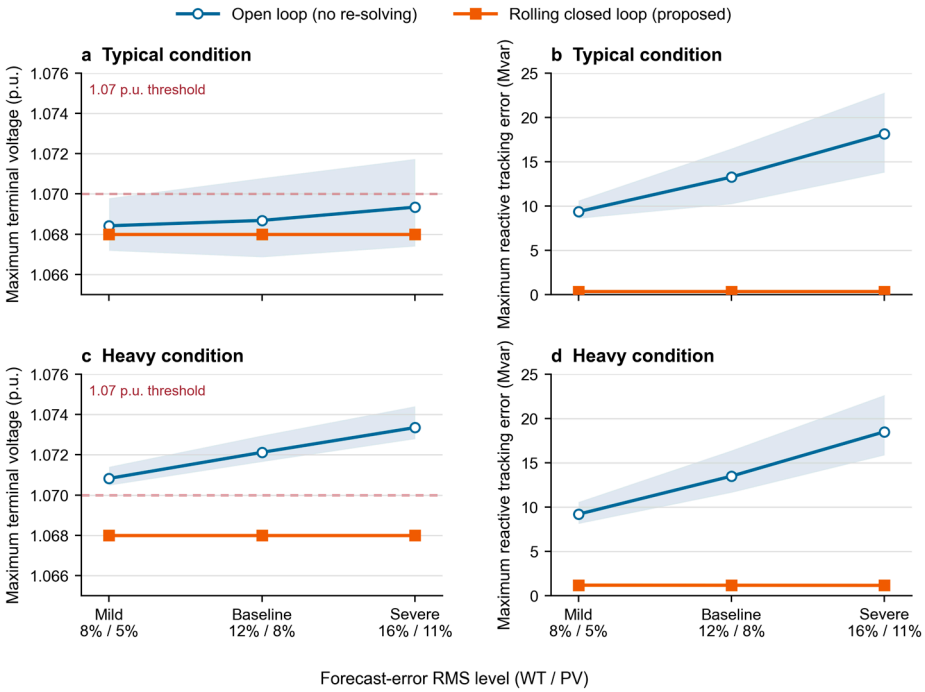


Figure A1. Sensitivity of the maximum terminal voltage and maximum reactive tracking error to the forecast-error RMS level under the typical and heavy operating conditions. The solid lines show the mean over three independent AR(1) forecast-error realizations, and the shaded bands show the observed minimum–maximum range.

The sensitivity results show that open-loop execution becomes increasingly affected by the renewable-generation forecast error, particularly under the heavy operating condition. Rolling re-optimization substantially reduces both the magnitude and the realization-to-realization variation in the reactive tracking error while maintaining the terminal-voltage limit throughout the tested uncertainty range.

Appendix C. Weight-Coefficient Sensitivity Analysis

A one-at-a-time sensitivity analysis was performed to quantify the influence of the objective-weight selection on the optimization results. Five coefficient groups were considered: (1) the active- and reactive-power tracking coefficients, (2) the network-loss coefficient, (3) the curtailment coefficient, (4) the reactive-source-cost coefficient, and (5) the high-voltage-branch regularization coefficient. Each coefficient group was independently scaled to 0.5, 1.0, and 2.0 times its reference value, while the remaining coefficients and all operating parameters were kept unchanged.

The analysis was conducted over the four-step, 1 h evening-peak optimization window beginning at time step 76. Two representative operating conditions were considered. The typical condition has a peak reactive-power demand of 120 Mvar, whereas the heavy condition has a peak reactive-power demand of 155 Mvar. The combination of five coefficient groups, three scaling factors, and two operating conditions resulted in 30 deterministic optimization cases.

As shown in Figure A2a, the active- and reactive-power tracking errors decrease consistently as the corresponding tracking coefficients increase. Under the typical condition, increasing the tracking-coefficient scaling factor from 0.5 to 2.0 reduces the maximum active-power tracking error from 1.035 to 0.259 MW and the maximum reactive-power tracking error from 0.579 to 0.145 Mvar. Under the heavy condition, the corresponding errors decrease from 1.045 to 0.262 MW and from 1.108 to 0.283 Mvar, respectively. These results confirm that the tracking coefficients directly and consistently control command-following accuracy.

Figure A2b shows the principal trade-off between modeled network losses and renewable-energy curtailment. When the network-loss coefficient increases from 0.5 to 2.0 times its reference value, the modeled loss rate decreases from 3.284% to 1.741% under the typical condition, while curtailed energy increases from 0.471 to 229.367 MWh. Under the heavy condition, the modeled loss rate decreases from 3.031% to 1.779%, while curtailed energy increases from 31.972 to 226.038 MWh. The curtailment coefficient produces the opposite trajectory. Increasing this coefficient from 0.5 to 2.0 times its reference value reduces curtailed energy from 229.192 to 0.333 MWh under the typical condition and from 224.852 to 30.142 MWh under the heavy condition, accompanied by increases in the modeled loss rate from 1.744% to 3.284% and from 1.802% to 3.045%, respectively. The reference setting occupies an intermediate position along both trajectories and therefore provides an appropriate balance between network efficiency and renewable-energy utilization.

As shown in Figure A2c, variations in the reactive-source-cost coefficient have a smaller effect than variations in the tracking, network-loss, and curtailment coefficients. Under the typical condition, the maximum reactive-power tracking error remains approximately 0.290 Mvar, and curtailed energy varies only from 74.322 to 74.566 MWh. Under the heavy condition, increasing the coefficient scaling factor from 0.5 to 2.0 changes the maximum reactive-power tracking error from 0.519 to 0.650 Mvar and curtailed energy from 85.168 to 96.010 MWh. This operating-condition-dependent response confirms that the reactive-source-cost term provides secondary refinement, particularly when the system is subjected to a higher reactive-power demand.

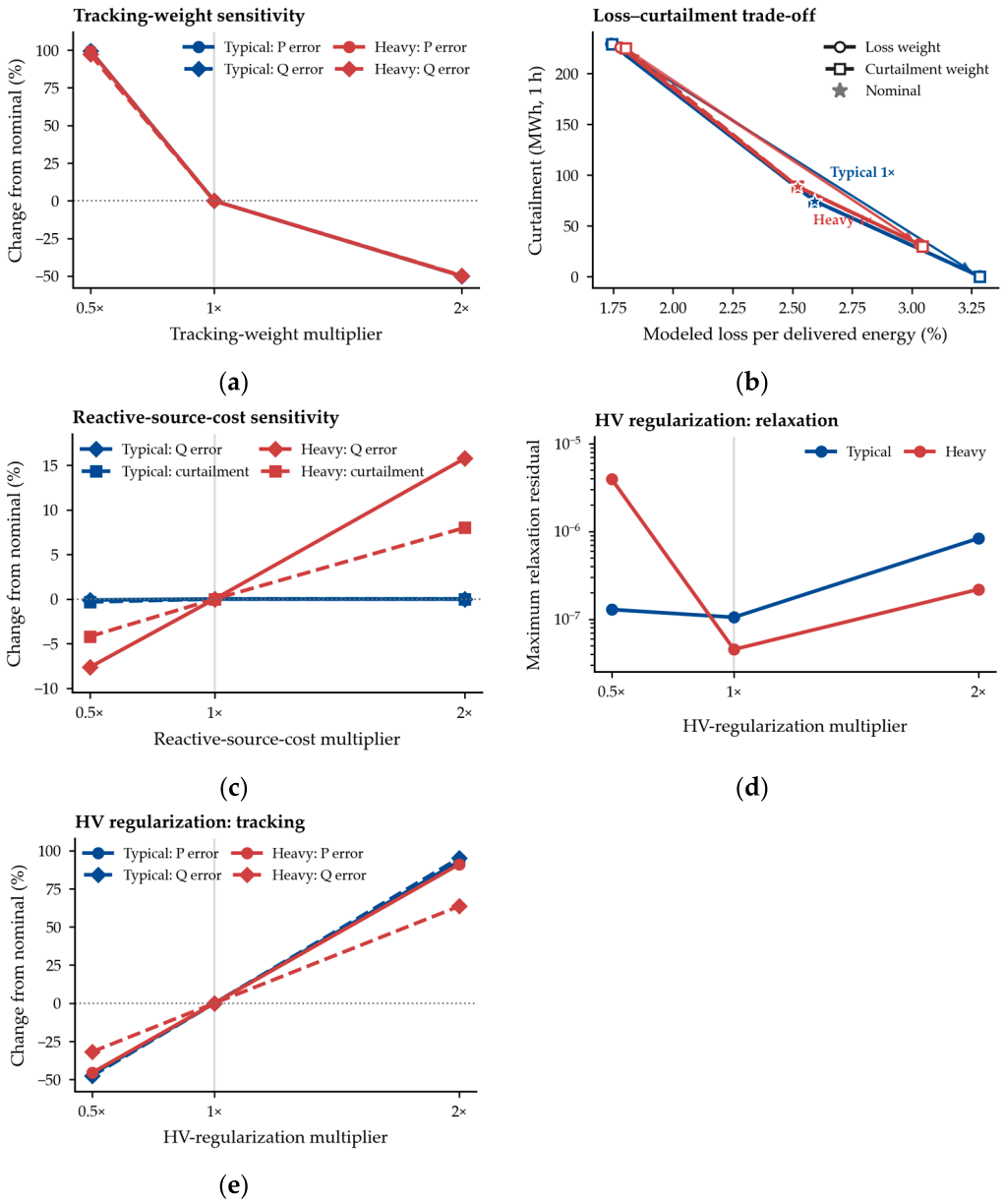


Figure A2. Sensitivity of the optimization results to the objective-weight groups under typical and heavy evening-peak operating conditions. (**a**) Relative changes in the maximum active- and reactive-power tracking errors when the tracking coefficients are varied. The reference active/reactive tracking errors are 0.518 MW/0.290 Mvar under the typical condition and 0.523 MW/0.562 Mvar under the heavy condition. (**b**) Network-loss–curtailment trajectories obtained by varying the network-loss and curtailment coefficients. The arrows indicate an increase in the scaling factor from 0.5 to 2.0, and the stars denote the reference setting. (**c**) Relative changes in the maximum reactive-power tracking error and curtailed energy when the reactive-source-cost coefficient is varied. (**d**) Maximum relaxation residual obtained by varying the high-voltage-branch regularization coefficient. (**e**) Relative changes in the active- and reactive-power tracking errors associated with the high-voltage-branch regularization coefficient. Each point represents one deterministic optimization result. Blue and red denote the typical and heavy operating conditions, respectively; marker shapes distinguish the corresponding metrics, as indicated in the panel legends.

Figure A2d,e illustrate the influence of the high-voltage-branch regularization coefficient. At the reference setting, the maximum relaxation residual is 1.05×10^{-7} under the typical condition and 4.52×10^{-8} under the heavy condition, representing the smallest residual among the three tested settings for both conditions. The reference coefficient

therefore provides strong numerical tightness while maintaining satisfactory active- and reactive-power tracking performance.

Overall, the sensitivity analysis confirms the intended hierarchy of the objective function. The tracking coefficients primarily control command-following accuracy, the network-loss and curtailment coefficients define the main operational trade-off, and the reactive-source-cost and high-voltage-branch regularization coefficients provide secondary operational and numerical refinement. The reference coefficient set achieves a balanced solution under both typical and heavy operating conditions while preserving terminal-voltage feasibility and a small relaxation gap.

References

1. Zhao, Y.; Zhong, H.; Kong, F.; Zhang, N. Can China achieve carbon neutrality without power shortage? A substitutability perspective. *Renew. Sustain. Energy Rev.* **2023**, *182*, 113402. [CrossRef]
2. Wang, Y.; Yang, Z.; Li, Y.; Dong, H.; Xing, J. Integrated planning of source-grid-load-storage for regional power grids considering large-scale renewable energy integration. *Energy* **2026**, *345*, 140146. [CrossRef]
3. Huang, K.; Liu, P.; Ming, B.; Kim, J.S.; Gong, Y. Economic operation of a wind-solar-hydro complementary system considering risks of output shortage, power curtailment and spilled water. *Appl. Energy* **2021**, *290*, 116805. [CrossRef]
4. Wen, S.; Gong, Y.; Mu, X.; Zhao, S.; Wang, C. Optimal configuration of flywheel–battery hybrid energy storage system for smoothing wind–solar power generating fluctuation. *Energies* **2025**, *18*, 2055. [CrossRef]
5. Niu, Y.; Meng, M.; Li, X.; Pang, T. Operational decisions of wind–photovoltaic–storage hybrid power systems using improved dung beetle optimizer. *J. Energy Storage* **2025**, *117*, 116225. [CrossRef]
6. Zhao, C.; Andersen, P.B.; Træholt, C.; Hashemi, S. Grid-connected battery energy storage system: A review on application and integration. *Renew. Sustain. Energy Rev.* **2023**, *182*, 113400. [CrossRef]
7. Wang, W.; Li, G.; Guo, J. Large-scale renewable energy transmission by HVDC: Challenges and proposals. *Engineering* **2022**, *19*, 252–267. [CrossRef]
8. Shen, Z.; He, Z.; Nian, H.; Wen, C.; Lin, X.; Lu, K.; Wei, W.; Chen, Z. Overstresses coupling mechanism and coordinated suppression strategy of ultra-long MMC-HVDC system under DC overhead line fault. *IEEE Trans. Power Electron.* **2026**, *early access*. [CrossRef]
9. He, Z.; Lu, M.; Hang, L.; Zeng, P.; Liu, Y. Capacitor voltage imbalance mechanism and balancing control of MMC when riding through PTG fault. *CSEE J. Power Energy Syst.* **2024**, *10*, 778–785. [CrossRef]
10. He, Z.; Hu, J.; Lin, L.; Zeng, P.; Hang, L. A generalized DC asymmetrical fault analysis method for MMC-HVDC grids considering metallic return conductors. *IEEE Trans. Power Deliv.* **2024**, *39*, 2568–2579. [CrossRef]
11. Li, X.; Qu, Y.; Deng, J.; Huang, S.; Luo, D.; Wu, Q. Distributed Optimal Voltage Control for Multi-terminal Direct Current System with Large-scale Wind Farm Cluster Based on ADMM. *J. Mod. Power Syst. Clean Energy* **2024**, *13*, 1052–1063. [CrossRef]
12. Karaagac, U.; Kocar, I.; Mahseredjian, J.; Cai, L.; Javid, Z. STATCOM integration into a DFIG-based wind park for reactive power compensation and its impact on wind park high voltage ride-through capability. *Electr. Power Syst. Res.* **2021**, *199*, 107368. [CrossRef]
13. Oliveira, M.C.; Ramos, R.A.; Costa-Alberto, L.F.; Grilo-Pavani, A.P. A probabilistic approach to voltage security assessment with high penetration of renewable generation. *IEEE Trans. Sustain. Energy* **2026**, *17*, 1161–1172. [CrossRef]
14. Zhang, G.; Hu, W.; Cao, D.; Zhou, D.; Huang, Q.; Chen, Z.; Blaabjerg, F. Coordinated active and reactive power dynamic dispatch strategy for wind farms to minimize levelized production cost considering system uncertainty: A soft actor-critic approach. *Renew. Energy* **2023**, *218*, 119335. [CrossRef]
15. Corrêa, H.P.; Vieira, F.H.T. Hybrid cooperative Markov-based method for decentralized voltage control and loss reduction via photovoltaic reactive power support. *Electr. Power Syst. Res.* **2024**, *232*, 110398. [CrossRef]
16. Takagi, M.; Fukushima, K.; Tagashira, N.; Okada, K.; Asano, H. Cost-effectiveness analysis method for voltage stabilization in case of combining storage battery and reactive power compensator. *J. Energy Storage* **2024**, *93*, 112065. [CrossRef]
17. Peng, Y.; Wang, H.; Zhao, Q.; Nan, D.; Li, W. Research and application of combined reactive power compensation device based on SVG+SC in wind power gathering area. *Appl. Sci.* **2022**, *12*, 10906. [CrossRef]
18. Zhou, S.; Rong, F.; Ning, X. Optimization control strategy for large doubly-fed induction generator wind farm based on grouped wind turbine. *Energies* **2021**, *14*, 4848. [CrossRef]
19. Dai, J.; Wan, L.; Chang, P.; Liu, L.; Zhou, X. Reactive voltage control strategy for PMSG-based wind farm considering reactive power adequacy and terminal voltage balance. *Electronics* **2022**, *11*, 1766. [CrossRef]
20. Fan, X.; Crisostomi, E.; Thomopulos, D.; Zhang, B.; Shorten, R.; Yang, S. An optimized decentralized power sharing strategy for wind farm de-loading. *IEEE Trans. Power Syst.* **2021**, *36*, 136–146. [CrossRef]

21. Li, G.; Zhang, W.; Zhao, Q.; Wei, M.; Shen, L.; Zhou, Q.; Gao, Y. Coordinated reactive power optimal control considering the voltage security of wind farm. *IET Smart Grid* **2025**, *8*, e70009. [CrossRef]
22. Rong, F.; He, L.; Huang, S.; Lyu, M.; He, C.; Li, X.; Zhao, C. A split Bregman method solving optimal reactive power dispatch for a doubly-fed induction generator-based wind farm. *Sci. Rep.* **2022**, *12*, 19222. [CrossRef] [PubMed]
23. Han, J.; Zhang, D.; Jia, B.; Xie, L.; Wan, W.; Tan, J.; Chen, Z. Power loss minimization-oriented reactive power control for wind farm equipped with distributed energy storages using clustering-based data-driven method. *Energy* **2025**, *328*, 136599. [CrossRef]
24. Li, Y.; Zhu, G.; Lu, J.; Geng, H. Hierarchical coordinated voltage control for wind farm with wind speed fluctuations. *Electr. Power Syst. Res.* **2026**, *250*, 112125. [CrossRef]
25. Kuang, H.; Su, F.; Chang, Y.; Wang, K.; He, Z. Reactive power optimization for distribution network system with wind power based on improved multi-objective particle swarm optimization algorithm. *Electr. Power Syst. Res.* **2022**, *213*, 108731. [CrossRef]
26. Varan, M.; Erduman, A.; Menevşeoğlu, F. A grey wolf optimization algorithm-based optimal reactive power dispatch with wind-integrated power systems. *Energies* **2023**, *16*, 5021. [CrossRef]
27. Song, Y.; Hill, D.J.; Liu, T.; Chen, T. Convex relaxation of AC optimal power flow with flexible transmission line impedances. *IEEE Trans. Power Syst.* **2022**, *37*, 3129–3132. [CrossRef]
28. Gan, L.; Li, N.; Topcu, U.; Low, S.H. Exact convex relaxation of optimal power flow in radial networks. *IEEE Trans. Autom. Control* **2015**, *60*, 72–87. [CrossRef]
29. Zhou, Y.; Wang, Q.; Huang, T.; Liao, J.; Chi, Y.; Zhou, N.; Xu, X.; Zhang, X. Convex optimal power flow based on power injection-based equations and its application in bipolar DC distribution network. *Electr. Power Syst. Res.* **2024**, *230*, 110271. [CrossRef]
30. Niu, T.; Liu, H.; Guo, Q.; Lan, H.; Sun, H.; Wang, Y.; Wang, B.; Liu, X. Wind farm side optimal power flow based on DistFlow and SOCP: Model and case study. In *2014 IEEE PES Asia-Pacific Power and Energy Engineering Conference (APPEEC)*; IEEE: New York, NY, USA, 2014; pp. 1–5. [CrossRef]
31. Martin, B.; Glineur, F.; De Rua, P.; De Jaeger, E. Loss reduction in a windfarm participating in primary voltage control using an extension of the convex DistFlow OPF. In *2018 Power Systems Computation Conference (PSCC)*; IEEE: New York, NY, USA, 2018; pp. 1–8. [CrossRef]
32. Cui, H.; Li, X.; Wu, G.; Song, Y.; Liu, X.; Luo, D. MPC based coordinated active and reactive power control strategy of DFIG wind farm with distributed ESSs. *Energies* **2021**, *14*, 3906. [CrossRef]
33. Huang, S.; Gong, Y.; Wu, Q.; Rong, F. Two-tier combined active and reactive power controls for VSC–HVDC-connected large-scale wind farm cluster based on ADMM. *IET Renew. Power Gener.* **2020**, *14*, 1379–1386. [CrossRef]
34. Ma, K.; Chen, Y.; Wang, S.; Wang, Q.; Sun, K.; Fan, W.; Nian, H.; Wei, J. Coordinated voltage control for large-scale wind farms with ESS and SVG based on MPC considering wake effect. *Front. Energy Res.* **2024**, *12*, 1443626. [CrossRef]
35. Zhou, B.; Wang, Y.; Xu, Y.; Jiang, X.; Yu, B.; Nian, H.; He, Z. Two-layer coordinated optimization and control method for wind farms considering both point of common coupling voltage level and generator terminal voltage security. *Energies* **2026**, *19*, 771. [CrossRef]
36. Du, M.; Zhang, X.; Zhang, J.; Zhang, R.; Zhao, J. Robust Resilience Enhancement Strategy Against Uncertain Cyber-Physical Coordinated Attacks Considering Power-Communication Network Interdependence. *IEEE Trans. Power Syst.* **2026**, *41*, 2879–2894. [CrossRef]

Disclaimer/Publisher's Note: The statements, opinions and data contained in all publications are solely those of the individual author(s) and contributor(s) and not of MDPI and/or the editor(s). MDPI and/or the editor(s) disclaim responsibility for any injury to people or property resulting from any ideas, methods, instructions or products referred to in the content.